



**A dynamic marine iron cycle for the UVic model**

L. Nickelsen et al.

# A dynamic marine iron cycle module coupled to the University of Victoria Earth System Model: the Kiel Marine Biogeochemical Model 2 (KMBM2) for UVic 2.9

L. Nickelsen, D. P. Keller, and A. Oschlies

GEOMAR Helmholtz-Zentrum für Ozeanforschung Kiel, Düsternbrooker Weg 20,  
24105 Kiel, Germany

Received: 15 October 2014 – Accepted: 11 November 2014 – Published: 5 December 2014

Correspondence to: L. Nickelsen (lnickelsen@geomar.de)

Published by Copernicus Publications on behalf of the European Geosciences Union.

Title Page

Abstract

Introduction

Conclusions

References

Tables

Figures



Back

Close

Full Screen / Esc

Printer-friendly Version

Interactive Discussion



## Abstract

Marine biological production and the associated biotic uptake of carbon in many ocean regions depend on the availability of nutrients in the euphotic zone. While large areas are limited by nitrogen and/or phosphorus, the micronutrient iron is considered the main limiting nutrient in the North Pacific, equatorial Pacific and Southern Ocean. Changes in iron availability via changes in atmospheric dust input are discussed to play an important role in glacial/interglacial cycles via climate feedbacks caused by changes in biological ocean carbon sequestration. Although many aspects of the iron cycle remain unknown, its incorporation into marine biogeochemical models is needed to test our current understanding and better constrain its role in the Earth system. In the University of Victoria Earth System Climate Model (UVic) iron limitation in the ocean was, until now, simulated pragmatically with an iron concentration masking scheme that did not allow a consistent interactive response to perturbations of ocean biogeochemistry or iron cycling sensitivity studies. Here, we replace the iron masking scheme with a dynamic iron cycle and compare the results to available observations and the previous marine biogeochemical model. Sensitivity studies are also conducted with the new model to test the importance of considering the variable solubility of iron in dust deposition, the importance of considering high resolution bathymetry for the sediment release of iron, the effect of scaling the sedimentary iron release with temperature and the sensitivity of the iron cycle to a climate change scenario.

## 1 Introduction

The Earth system consists of three major components: ocean, atmosphere and land. All of them interact and shape the Earth's climate. Understanding the most important dynamics and the way they influence the climate is an urgent task because of mankind's dependence on, and increasing interference with, the climate of our planet. The ocean is a particularly important component of the Earth system since it has the

GMDD

7, 8505–8563, 2014

## A dynamic marine iron cycle for the UVic model

L. Nickelsen et al.

Title Page

Abstract

Introduction

Conclusions

References

Tables

Figures



Back

Close

Full Screen / Esc

Printer-friendly Version

Interactive Discussion



## A dynamic marine iron cycle for the UVic model

L. Nickelsen et al.

Title Page

Abstract

Introduction

Conclusions

References

Tables

Figures



Back

Close

Full Screen / Esc

Printer-friendly Version

Interactive Discussion



capacity to compensate for large fluctuations of the greenhouse gas CO<sub>2</sub> in the atmosphere. For instance, Sabine et al. (2004) estimated that the global oceanic anthropogenic CO<sub>2</sub> sink for the period from 1800 to 1994 accounts for 48 % of the total fossil-fuel and cement-manufacturing emissions. The oceanic uptake of anthropogenic carbon is thought to have, until now, occurred predominantly through the solubility pump, which describes the physical dissolution of CO<sub>2</sub> in sea water, a strongly temperature dependent process with more CO<sub>2</sub> being absorbed into cold, high latitude waters that sink into the ocean interior. So far, there is little evidence for changes in the so-called biological pump that transfers carbon from the surface ocean via phytoplankton uptake and sinking of organic matter to the deeper ocean. The biological pump does, however, have a huge potential to affect the partitioning of carbon between the ocean and the atmosphere. Its strength in many regions depends on nutrient limitation of phytoplankton so that ocean biogeochemistry has an influence on the global carbon cycle and climate.

Over the last two decades iron has been discovered to play an important role in ocean biogeochemistry. The availability of iron limits phytoplankton growth in the North Pacific, equatorial Pacific and Southern Ocean (Boyd and Ellwood, 2010). Dust deposition and more recently, sediment release of iron are seen as the major sources of iron to the ocean. Increases in Southern Ocean dust deposition are still discussed as possibly contributing to glacial/interglacial changes in atmospheric CO<sub>2</sub> concentrations by reducing Southern Ocean iron limitation (Martinez-Garcia et al., 2014). On the other hand, Tagliabue et al. (2014a) find in a modeling study that without sediment release of iron, the atmospheric CO<sub>2</sub> concentration would be 10.0–18.2 ppm higher. Furthermore, iron is particularly important for nitrogen fixing phytoplankton, so called diazotrophs that have a strong impact on the balance of the ocean nitrogen inventory (Mills et al., 2004; Moore and Doney, 2007; Somes et al., 2010). Thus, the marine iron cycle is an important part of the Earth system.

Earth system models are well suited for investigating the dynamics and sensitivities of the earth system to perturbations. However, Earth system and global ocean-only

## A dynamic marine iron cycle for the UVic model

L. Nickelsen et al.

Title Page

Abstract

Introduction

Conclusions

References

Tables

Figures



Back

Close

Full Screen / Esc

Printer-friendly Version

Interactive Discussion



models have usually incorporated simple representations of the iron cycle, such as in Moore and Braucher (2008), Parekh et al. (2008), and Tagliabue et al. (2014a). This level of complexity is useful for example, for investigating the sensitivity of oceanic CO<sub>2</sub> uptake to dust deposition or for comparing the role of sedimentary iron release to that of aeolian iron deposition. However, these models can have quite different sensitivities and a comparison of the models and their assumptions can indicate the reasons for the different sensitivities (Tagliabue et al., 2008). More mechanistic models are needed to identify the important processes and their sensitivities to environmental changes, and to reduce uncertainties in the model simulations.

In the University of Victoria Earth System Climate Model (UVic), which we use in this study, iron limitation has either been ignored (Schmittner et al., 2008) or modeled with the use of a non-dynamic iron masking scheme (Keller et al., 2012) that was based on iron concentrations calculated by another model (Galbraith et al., 2010), which contained a dynamic iron cycle. Thus, the iron concentrations in the most recent version of the marine biogeochemical component (Keller et al., 2012) are not interactive with the rest of the model. Furthermore, sensitivity studies and experiments that require dynamic feedbacks of the iron cycle from changes in biogeochemistry and physics cannot be carried out with a constant iron concentration mask. Here, we add a dynamic iron cycle to the UVic marine biogeochemical model to create the ability to investigate the iron cycle itself, the interactions of the iron cycle with other biogeochemical cycles and the climate. Our results indicate the importance of including the variable solubility of dust-deposited iron and the importance of the depth of sedimentary iron release to the water column. We also find that scaling the benthic iron release with temperature increases the agreement between simulated and observed iron concentrations in the Southern Ocean. The new model allows us to provide an estimate of global marine iron fluxes and shows how implementing the dynamic iron cycle improves the agreement of simulated ocean tracers with observations. Finally, the dynamic response of the iron cycle during a climate change scenario simulation is demonstrated.

## 2 Model description

A dynamic iron cycle is added to the Kiel Marine Biogeochemical Model (KMBM) by Keller et al. (2012) and coupled to the UVic version 2.9 (Eby et al., 2009, 2013; Weaver et al., 2001). The UVic model and the ocean biogeochemical model are briefly outlined before the new dynamic iron cycle is described.

### 2.1 The University of Victoria Earth System Climate Model

The UVic model (Eby et al., 2009, 2013; Weaver et al., 2001) is a climate model of intermediate complexity with the advantage of relatively low computational costs. The model consists of three components: a simple one layer atmospheric model, a terrestrial model and a three dimensional ocean circulation model. The horizontal grid resolution of all model components is  $3.6^\circ$  in meridional and  $1.8^\circ$  in latitudinal direction. The atmospheric component is an energy-moisture balance model that dynamically calculates heat and water fluxes between the atmosphere and the ocean, land and sea ice. Advection of water vapor in the atmosphere is calculated using monthly climatological wind data from the National Center for Atmospheric Research/National Center for Environmental Prediction (NCAR/NCEP). The land vegetation model is the terrestrial model of vegetation and carbon cycles (Meissner et al., 2003) based on the Hadley Center model TRIFFID. Land processes are modelled via the MOSES1 land surface exchange scheme (Cox, 2001). Continental ice sheets are assumed to be constant in our model configuration. In contrast, sea-ice is calculated with a thermo-dynamic sea-ice model. The ocean component is the Modular Ocean Model 2 (MOM2) and consists of 19 vertical layers and, as with the atmospheric component, is forced by monthly climatological wind data from NCAR/NCEP. Subgrid-scale eddy mixing is parameterized according to Gent and McWilliams (1990), the vertical diffusivity parameter in the Southern Ocean is increased as in Keller et al. (2012), tidally induced diapycnal mixing over rough topography is computed according to the scheme by Simmons et al. (2004), and an anisotropic viscosity scheme (Large et al., 2001) is applied in the tropics.

GMDD

7, 8505–8563, 2014

## A dynamic marine iron cycle for the UVic model

L. Nickelsen et al.

Title Page

Abstract

Introduction

Conclusions

References

Tables

Figures

◀

▶

◀

▶

Back

Close

Full Screen / Esc

Printer-friendly Version

Interactive Discussion



## 2.2 The marine biogeochemical model

The marine biogeochemical model used here was developed and extended by Oschlies and Garçon (1999), Schmittner et al. (2005), Schmittner et al. (2008) and Keller et al. (2012). The model is a NPZD type of model with nutrients, phytoplankton, zooplankton and detritus. Sources and sinks are described in the following and illustrated in Fig. 1a, for the full equations see Schmittner et al. (2008); Keller et al. (2012).

The model is nitrogen-based, but has two dissolved inorganic nutrient pools, nitrate ( $\text{NO}_3$ ) and phosphate ( $\text{PO}_4$ ). Redfield stoichiometry is used to convert the tracer mass into carbon, phosphorus, or oxygen when necessary. There are two types of phytoplankton, one of which represents nitrogen fixing phytoplankton types (diazotrophs,  $P_D$ ). Since they can fix dinitrogen into bioavailable forms, these diazotrophs are not limited by nitrate concentrations. In contrast, the other phytoplankton class ( $P_O$ ), which represents all non-nitrogen fixing phytoplankton, is limited by nitrate and phosphate. Microbial loop dynamics and dissolved organic matter cycling are parameterized via a fast recycling scheme that directly returns a fraction of phytoplankton into inorganic nutrients. Non-grazing related phytoplankton mortality also results in the production of detritus. Zooplankton (Z) graze on ordinary phytoplankton, diazotrophs, themselves and detritus (D). Growth and assimilation efficiency terms determine the fraction of prey biomass that is assimilated into biomass, respired, excreted or lost to detritus via sloppy feeding, egestion, and fecal pellet production. Zooplankton mortality also produces detritus. Detritus is considered as a tracer with horizontal advection and diffusion, but primarily sinks through the water column. A temperature-dependant function simulates microbial decomposition and remineralization to convert detritus back into inorganic nutrients and carbon. At the seafloor all detritus is instantly converted back into inorganic nutrients and carbon to simulate benthic decomposition and remineralization. During the remineralization of detritus, oxygen ( $\text{O}_2$ ), which is also a dynamically calculated tracer, is consumed. When oxygen levels fall below a threshold of  $5 \text{ mmol m}^{-3}$ , anaerobic remineralization sets in at rates 3 times slower than aerobic remineralization, and

GMDD

7, 8505–8563, 2014

### A dynamic marine iron cycle for the UVic model

L. Nickelsen et al.

Title Page

Abstract

Introduction

Conclusions

References

Tables

Figures



Back

Close

Full Screen / Esc

Printer-friendly Version

Interactive Discussion



with associated nitrogen losses representing the combined effects of denitrification and anammox.

Using fixed Redfield ratios between carbon and nitrogen, dissolved inorganic carbon and alkalinity are also included in the model. For a more complete description of the biogeochemical model also see the complete model code in the Supplement or at [https://thredds.geomar.de/thredds/fileServer/peerReviewData/nickelsen-et-al\\_gmd\\_2014/Nickelsen-et-al\\_GMD\\_2014\\_submitted.zip](https://thredds.geomar.de/thredds/fileServer/peerReviewData/nickelsen-et-al_gmd_2014/Nickelsen-et-al_GMD_2014_submitted.zip).

## 2.3 The new dynamic iron cycle

The iron cycle described here (Fig. 1b) largely follows Parekh et al. (2004, 2005) and Galbraith et al. (2010). Sources and sinks of the modeled iron cycle are explained first with description of parameterizations for iron limitation, scavenging, remineralization, sediment release and dust deposition given in the subsequent sections.

### 2.3.1 Sources and sinks of iron

The iron cycle is simulated with the addition of two new physical tracers, dissolved iron (Fe) and particulate iron (Fe<sub>p</sub>), to the marine biogeochemical model. The dissolved iron includes free iron and complexed iron, both of which are assumed to be entirely bioavailable.

The concentration of each tracer changes according to the following equation:

$$\frac{\partial C}{\partial t} = Tr + S \quad (1)$$

where Tr denotes physical transport including advection, isopycnal and diapycnal diffusion. S represents the source minus sink terms. All dissolved iron (Fe) is assumed to be bioavailable whereas particulate iron (Fe<sub>p</sub>) is not. Dissolved iron is taken up by phytoplankton and remineralized by grazing or microbial decomposition processes, biotically derived particulate iron is produced whenever organic detritus is produced.

## A dynamic marine iron cycle for the UVic model

L. Nickelsen et al.

Title Page

Abstract

Introduction

Conclusions

References

Tables

Figures

⏪

⏩

◀

▶

Back

Close

Full Screen / Esc

Printer-friendly Version

Interactive Discussion



These biotic fluxes are calculated from the nitrogen-based rates using a fixed Fe:N ratio ( $R_{\text{Fe:N}}$ ) (Table 1). The usage of a fixed Fe:N ratio is a pragmatic choice that reduces computational costs as it circumvents the need to calculate iron concentrations within each biological tracer. The sources and sinks of the two additional iron tracers are described by:

$$S(\text{Fe}) = R_{\text{Fe:N}}(\mu_P P_O + (\gamma - \bar{\omega})(\text{graz}_P + \text{graz}_D + \text{graz}_{\text{Det}} + \text{graz}_Z) - J_O P_O - J_D P_D) + \mu_{\text{Fe}_P} - \text{fe}_{\text{orgads}} - \text{fe}_{\text{prp}} + \text{fe}_{\text{sed}} + \text{fe}_{\text{dust}} \quad (2)$$

$$S(\text{Fe}_P) = R_{\text{Fe:N}}((1 - \gamma)(\text{graz}_P + \text{graz}_D + \text{graz}_{\text{Det}} + \text{graz}_Z) + \text{morp} + \text{morp}_D + \text{morz} - \text{graz}_{\text{Det}}) - \mu_{\text{Fe}_P} + \text{fe}_{\text{orgads}} + \text{fe}_{\text{prp}} - w_D \frac{\partial \text{Fe}_P}{\partial z} \quad (3)$$

The first term in Eq. (2), ( $\mu_P P_O$ ), is a temperature-dependent fast remineralization function that represents recycling of iron bound to phytoplankton-derived organic matter via the microbial loop and dissolved organic matter cycling. The second term represents iron excretion by zooplankton, which is calculated as the difference between their assimilation and growth efficiency coefficients ( $\gamma - \bar{\omega}$ ) for the sum of all grazing on phytoplankton ( $\text{graz}_P$ ), diazotrophs ( $\text{graz}_D$ ), detritus ( $\text{graz}_{\text{Det}}$ ) and themselves ( $\text{graz}_Z$ ). The third and fourth terms represent the uptake of dissolved iron by ordinary phytoplankton and diazotrophs ( $J_O P_O, J_D P_D$ ). The fifth term, ( $\mu_{\text{Fe}_P}$ ), represents the temperature-dependent decomposition and remineralization of particle bound iron. The next two terms represent abiotic iron cycling, which is characterized by the loss of bioavailable, dissolved iron through scavenging. Scavenging is modeled here as two distinct processes: adsorption of iron to organic material ( $\text{fe}_{\text{orgads}}$ ) and precipitation and colloidal formation with subsequent aggregation ( $\text{fe}_{\text{prp}}$ ) described in detail below. The final two terms represent the external sources of iron that are added to the water column from sediment release ( $\text{fe}_{\text{sed}}$ ) and dust deposition ( $\text{fe}_{\text{dust}}$ ).

In Eq. (3) the biotic sources and sinks of particulate iron are equal to the sources and sinks of detritus (see Eq. (6) in Keller et al., 2012). Thus the first term, which is calculated as one minus the zooplankton assimilation efficiency ( $1 - \gamma$ ) for the sum of all

**A dynamic marine iron cycle for the UVic model**

L. Nickelsen et al.

Title Page

Abstract

Introduction

Conclusions

References

Tables

Figures



Back

Close

Full Screen / Esc

Printer-friendly Version

Interactive Discussion



## A dynamic marine iron cycle for the UVic model

L. Nickelsen et al.

Title Page

Abstract

Introduction

Conclusions

References

Tables

Figures

◀

▶

◀

▶

Back

Close

Full Screen / Esc

Printer-friendly Version

Interactive Discussion



grazing (see coefficients above), represents the production of iron containing detritus from sloppy feeding, egestion, or fecal pellet release. The next three terms represent the production of iron containing detritus from the mortality of ordinary phytoplankton ( $m_{P_O}P_O$ ), diazotrophs ( $m_{P_D}P_D$ ) and zooplankton ( $m_ZZ^2$ ). The fifth term accounts for the removal of particle-bound iron by zooplankton grazing ( $\text{graz}_{\text{Det}}$ ). The sixth term, ( $\mu_{\text{Fe}_P}$ ), represents the loss of particulate iron due to temperature-dependent decomposition and remineralization. The next two terms represent the abiotic scavenging fluxes ( $\text{fe}_{\text{orgads}}$  and  $\text{fe}_{\text{prp}}$ ) that add to the particulate iron pool. The final term,  $w_D \frac{\partial \text{Fe}_P}{\partial z}$ , accounts for the vertical sinking of particulate iron with a sinking speed  $w_D$  that increases linearly with depth (see Keller et al., 2012; Schmittner et al., 2008). Depending on the redox state of seafloor sediments, particulate iron that sinks to the bottom is either instantly remineralized or buried in the sediments (see Sect. 2.3.4).

### 2.3.2 Phytoplankton iron limitation

Iron limitations of ordinary and diazotrophic phytoplankton is described in terms of Monod functions as in Aumont and Bopp (2006). For ordinary phytoplankton the formulation of iron limitation is based on the observation that larger cells have higher iron half-saturation constants than smaller ones (Timmermans et al., 2004). As Aumont and Bopp (2006) we assume that an increase of phytoplankton biomass is mainly due to increases in cell size so that the half-saturation constant of iron limitation for ordinary phytoplankton varies with their biomass  $P_O$ :

$$P_1 = \min(P_O, P_{\text{max}}) \quad (4)$$

$$P_2 = \max(0, P_O - P_{\text{max}}) \quad (5)$$

$$k\text{Fe}_O = \frac{k\text{Fe}_{\text{min}}P_1 + k\text{Fe}_{\text{max}}P_2}{P_1 + P_2} \quad (6)$$

The three parameters used for this formulation from Aumont and Bopp (2006) are the phytoplankton biomass above which the iron uptake half-saturation constant starts to

## A dynamic marine iron cycle for the UVic model

L. Nickelsen et al.

Title Page

Abstract

Introduction

Conclusions

References

Tables

Figures

◀

▶

◀

▶

Back

Close

Full Screen / Esc

Printer-friendly Version

Interactive Discussion



increase,  $P_{\max}$ , and the minimum ( $kFe_{\min}$ ) and maximum iron uptake half saturation constants ( $kFe_{\max}$ ). The iron uptake half-saturation constant for diazotrophs ( $kFe_D$ ) is set as a non-varying parameter to reduce the number of parameters and to reflect the stronger constraint that iron imposes on the growth of small, diazotrophic phytoplankton (Mills et al., 2004; Moore and Doney, 2007). Using these half-saturation constants, iron limitation variables ( $felim_O$ ,  $felim_D$ ) for both, ordinary and diazotrophic phytoplankton are calculated:

$$felim_O = \frac{Fe}{kFe_O + Fe}, \quad (7)$$

$$felim_D = \frac{Fe}{kFe_D + Fe}. \quad (8)$$

Then as in Keller et al. (2012), these limiting variables are included in the calculation of the potential phytoplankton maximum growth rates to reflect the necessity of iron for photosynthesis, the reduction of nitrate to ammonium, and a number of other key cellular processes (Galbraith et al., 2010) (i.e., we assume that iron must be available before photosynthesis or the uptake and utilisation of nitrogen and phosphate is possible).

$$J_O^{\max} = a \exp(T/T_b) felim_O \quad (9)$$

$$J_D^{\max} = c_D \max(0, a \exp(T/T_b) - 2.61) felim_D \quad (10)$$

where the maximum growth at  $0^\circ\text{C}$  is multiplied with an e-folding temperature dependence term  $T/T_b$ , which produces a temperature constrained growth rate curve that is identical to the Eppley curve (Eppley, 1972) except at very high ocean temperatures, and the iron limitation variable. As in Schmittner et al. (2008) and Keller et al. (2012) diazotroph growth is reduced by using a handicap  $c_D$  and a stronger temperature dependence so that growth is inhibited below  $15^\circ\text{C}$ .

In addition to the constraints that iron limitation imposes on the maximum potential growth rate, iron is assumed to influence phytoplankton light harvesting capabilities.

Phytoplankton light limited growth is basically calculated as in Keller et al. (2012) and Schmittner et al. (2008) using

$$J_{(O \text{ or } D)l} = \frac{J_{(O \text{ or } D)}^{\max} \alpha l}{\left[ \left( J_{(O \text{ or } D)}^{\max} \right)^2 + (\alpha l)^2 \right]^{1/2}} \quad (11)$$

For the full calculation of the depth averaged light limitation with a triangular shaped diurnal irradiance cycle see Schmittner et al. (2009) and Keller et al. (2012). Here the Eq. (11) for light limited growth is modified following Galbraith et al. (2010) by making the initial slope of the photosynthesis irradiance curve  $\alpha$  chlorophyll specific ( $\alpha^{\text{chl}}$ ) and making light limitation dependent on a Chl : C ratio  $\theta$ . Both,  $\alpha^{\text{chl}}$  and  $\theta$ , are in turn dependent on iron concentrations. In this way the dependence of light harvesting capabilities and chlorophyll synthesis on iron concentrations as suggested by field and culture experiments (Hopkinson et al., 2007; Price, 2005) is represented in the model. Thus, the phytoplankton light limited growth becomes

$$J_{(O \text{ or } D)l} = \frac{J_{(O \text{ or } D)}^{\max} \alpha^{\text{chl}} \theta_{(O \text{ or } D)} l}{\left[ \left( J_{(O \text{ or } D)}^{\max} \right)^2 + (\alpha^{\text{chl}} \theta_{(O \text{ or } D)} l)^2 \right]^{1/2}} \quad (12)$$

where  $J_{(O \text{ or } D)}^{\max}$  are the maximum potential growth rates and  $l$  is irradiance. The realized Chl : C ratios  $\theta_{(O \text{ or } D)}$  are calculated as

$$\theta_O = \theta_{\min} + (\theta_{\max} - \theta_{\min}) \text{felim}_O \quad (13)$$

$$\theta_D = \theta_{\min} + (\theta_{\max} - \theta_{\min}) \text{felim}_D \quad (14)$$

## GMDD

7, 8505–8563, 2014

### A dynamic marine iron cycle for the UVic model

L. Nickelsen et al.

Title Page

Abstract

Introduction

Conclusions

References

Tables

Figures



Back

Close

Full Screen / Esc

Printer-friendly Version

Interactive Discussion



and the initial slope of the PI-curve as

$$\alpha_{\text{O}}^{\text{chl}} = \alpha_{\text{min}}^{\text{chl}} + \left( \alpha_{\text{max}}^{\text{chl}} - \alpha_{\text{min}}^{\text{chl}} \right) \text{felim}_{\text{O}} \quad (15)$$

$$\alpha_{\text{D}}^{\text{chl}} = \alpha_{\text{min}}^{\text{chl}} + \left( \alpha_{\text{max}}^{\text{chl}} - \alpha_{\text{min}}^{\text{chl}} \right) \text{felim}_{\text{D}} \quad (16)$$

The iron limitation variables  $\text{felim}_{\text{O,D}}$  are used here to create a linear change between minimum and maximum parameter values following Galbraith et al. (2010). The impact of making  $\alpha^{\text{chl}}$  and  $\theta$  functions of iron concentrations is comprehensively described by Galbraith et al. (2010). They find that this formulation leads to increases in the agreement to observations of surface phosphate concentrations and export production, a more pronounced seasonal cycle of primary production and a stronger phytoplankton growth limitation in the Southern Ocean.

### 2.3.3 Iron scavenging and remineralization

Scavenging, which converts dissolved iron into colloidal and particulate forms, is an important part of the marine iron cycle. Iron speciation determines whether iron is subject to scavenging or stays dissolved as an organic complex bound to an organic ligand. Since the association and dissociation of iron to ligands occurs on time scales  $< 1$  day (Gledhill and Buck, 2012), we follow Parekh et al. (2004) in assuming that this process occurs rapidly enough so that a chemical equilibrium is reached between free iron, free ligands and organic iron complexes. Thus, we avoid the need to add computationally costly tracers for free ligands and organic iron complexes. As in Parekh et al. (2004) the concentration of free iron  $\text{Fe}_{\text{prime}}$  that is subject to scavenging can then be calculated from the following equations assuming a chemical equilibrium between

## GMDD

7, 8505–8563, 2014

### A dynamic marine iron cycle for the UVic model

L. Nickelsen et al.

Title Page

Abstract

Introduction

Conclusions

References

Tables

Figures

⏪

⏩

◀

▶

Back

Close

Full Screen / Esc

Printer-friendly Version

Interactive Discussion



free iron, free ligands and organic iron complexes.

$$L = \text{FeL} + L_{\text{prime}} \quad (17)$$

$$\text{Fe} = \text{FeL} + \text{Fe}_{\text{prime}} \quad (18)$$

$$K_{\text{FeL}} = \frac{\text{FeL}}{\text{Fe}_{\text{prime}}L_{\text{prime}}} \quad (19)$$

- 5 The total ligand concentration ( $L$ ) is assumed to be a globally constant model parameter due to uncertainties in the sources and sinks and to lower numerical costs. Ligand bound iron is denoted by  $\text{FeL}$ , the free ligand concentration by  $L_{\text{prime}}$ , the total dissolved iron concentration by  $\text{Fe}$  and the equilibrium constant between free iron and ligands and the organic complexes by  $K_{\text{FeL}}$ . Solving for  $\text{Fe}_{\text{prime}}$  gives

$$10 \text{Fe}_{\text{prime}} = \frac{-A + (A^2 + 4K_{\text{FeL}}\text{Fe})^{0.5}}{2K_{\text{FeL}}}, \quad (20)$$

$$A = 1 + K_{\text{FeL}}(L - \text{Fe}), \quad (21)$$

where the equilibrium constant  $K_{\text{FeL}}$  is considered a globally constant parameter whose value is based on a compilation by Gledhill and Buck (2012).

- 15 Once  $\text{Fe}_{\text{prime}}$  is known, scavenging can be calculated. The first scavenging process is the adsorption of free dissolved inorganic iron onto organic material. Following Parekh et al. (2005) and Galbraith et al. (2010) and based on the observations by Honeyman et al. (1988), the adsorption rate in the model ( $\text{fe}_{\text{orgads}}$ ) is dependent on the particulate organic matter concentration  $\text{Detr}$ , the concentration of free iron  $\text{Fe}_{\text{prime}}$  and the scavenging rate  $k\text{Fe}_{\text{org}}$ .

$$20 \text{fe}_{\text{orgads}} = k\text{Fe}_{\text{org}}\text{Fe}_{\text{prime}}(\text{Detr}R_{\text{C:N}}M_{\text{C}})^{0.58} \quad (22)$$

The carbon to nitrogen ratio is denoted by  $R_{\text{C:N}}$  and the molar mass of carbon by  $M_{\text{C}} = 12.011 \text{ g mol}^{-1}$ . In the second scavenging process ( $\text{fe}_{\text{prp}}$ ), iron precipitates and forms

colloids which can subsequently aggregate into larger particles. This more inorganic process is represented in the model using a linear scavenging rate that is independent of the organic particle concentration:

$$fe_{prp} = kFe_{prp}Fe_{prime} \quad (23)$$

5 The scavenging rate constant for precipitation, colloid formation and aggregation is denoted by  $kFe_{prp}$ . Both scavenging rates are set to zero when oxygen concentrations fall below a threshold  $O_{2min}$  (Table 1) as in the model by Galbraith et al. (2010) because iron oxidation rates are reduced and elevated iron concentrations are repeatedly observed under low oxygen concentrations (Hopkinson and Barbeau, 2007; Moffett et al., 10 2007; Rijkenberg et al., 2012).

Remineralization and sinking of particulate iron is proportional to that of particulate nitrogen (e.g., detritus). Thus, the temperature dependent remineralization rate is calculated as

$$\mu_{Fe_P} = \mu_{d0} \exp(T/T_b) Fe_P \quad (24)$$

15 where  $\mu_{d0}$  is the remineralization rate parameter for both particulate iron and particulate organic nitrogen at zero degrees C.

### 2.3.4 Sediment iron cycling

Observations of iron release or burial in sediments have shown that these processes are dependent on the sediment redox state, which is primarily determined by the oxygen content of the overlying water column (Noffke et al., 2012; Severmann et al., 20 2010), the ambient temperature (Arnosti et al., 1998; Sanz-Lázaro et al., 2011) and the amount of organic matter that reaches the sea floor and is remineralized therein (Elrod et al., 2004).

Here we follow the model of Galbraith et al. (2010) to calculate the flux of iron from the sediment. Iron is released with a constant ratio ( $Fe : P_{sed}$ ) of iron to particulate

organic phosphorus reaching the sediment ( $F_{POP}$ ). Particulate iron that sinks out of the bottom ocean layer is permanently removed from the ocean, as long as oxygen concentrations are greater than the suboxic threshold  $O_{2min}$  (cf. diagenesis in Fig. 1b). However, if bottom water oxygen concentrations are below  $O_{2min}$ , then the environment is assumed to be strongly reducing and the all particulate iron is released back into the water column, producing dissolved iron:

$$fe_{sed} = Fe : P_{sed} F_{POP} \exp(T/T_b) \quad (O_2 > O_{2min}), \quad (25)$$

$$fe_{sed} = Fe : P_{sed} F_{POP} \exp(T/T_b) + F_{Fe_p} \quad (O_2 \leq O_{2min}). \quad (26)$$

The ratio between iron released from the sediment and phosphorus in particulate matter that sinks into the sediment is denoted by  $Fe : P_{sed}$  and is based on the observation of such a constant ratio by Elrod et al. (2004). Due to the observation of temperature dependent remineralization (Arnosti et al., 1998; Sanz-Lázaro et al., 2011), the importance of sediment release for the iron reservoir and an improvement of agreement between our simulated and observed iron concentrations particularly in the Southern Ocean, we assume that remineralization of iron in the sediment is temperature dependent by multiplying with a temperature dependent factor ( $\exp(T/T_b)$  where  $T_b = 15.65^\circ\text{C}$ ). The average observed iron concentrations south of  $40^\circ\text{S}$  are 0.52 nM, simulated concentrations are 0.67 nM without and 0.53 nM with the temperature dependence. The assumption of temperature dependent iron release is tested and discussed further in Sect. 4. Riverine sources of iron are scavenged quickly at river mouths so that they are not viewed as an important source of iron to the ocean. Yet, the scavenged iron from rivers can reach the sediment and under low bottom water oxygen concentrations are released again as dissolved iron to the water column (Severmann et al., 2010). Equation (26) allows that locally, i.e. under bottom water oxygen concentrations smaller than  $O_{2min}$ , more iron can be released from the sediment than reaches it to reflect the massive iron release under low bottom water oxygen concentrations (Noffke et al., 2012) and implicitly also representing the riverine source of iron to the sediment.

**A dynamic marine iron cycle for the UVic model**

L. Nickelsen et al.

Title Page

Abstract

Introduction

Conclusions

References

Tables

Figures



Back

Close

Full Screen / Esc

Printer-friendly Version

Interactive Discussion





constant 1% solubility do not reproduce the solubility pattern and are thus considerably larger than the total iron deposition of  $2.1 \text{ Gmol Fe yr}^{-1}$  by Luo et al. (2008). At every ocean tracer time step we calculate the amount of iron that is deposited from the monthly values using linear interpolation (Fig. 2).

## 2.4 Parameter choices and spinup

Only the parameters associated with the iron cycle are new (Table 1). All other parameters are as in Keller et al. (2012). Whenever possible model parameters were based on observed values or taken from previously evaluated modelling studies. For parameters that are poorly constrained, the parameters were chosen within an observed range of values, if possible, to best simulate observed biogeochemical properties. The goal was to maximize agreement of surface macronutrients to observations and iron concentrations to the sparse observations while keeping the agreement of subsurface biogeochemical properties such as phosphate, nitrate and oxygen concentrations to observations similar to the agreement in the previous model version. Before the comparison to observations and the previous model version, the model was spun up for 10 000 years using preindustrial boundary conditions for insolation and a fixed atmospheric  $\text{CO}_2$  concentration of  $283 \mu\text{atm}$ .

## 3 Model evaluation

The evaluation in this section focuses exclusively on the iron cycle and the other biogeochemical properties of the model because the physical (Weaver et al., 2001) and terrestrial components (Meissner et al., 2003) have been evaluated in detail in previous studies. Comparisons to the World Ocean Atlas 2009 (WOA09) (Garcia et al., 2010a, b), and Global Data Analysis Project (GLODAP) (Key et al., 2004) and an iron concentration compilation database (Tagliabue et al., 2012) allow us to evaluate the performance of the model in terms of agreement to observations. The model is also

## A dynamic marine iron cycle for the UVic model

L. Nickelsen et al.

Title Page

Abstract

Introduction

Conclusions

References

Tables

Figures



Back

Close

Full Screen / Esc

Printer-friendly Version

Interactive Discussion



compared to the previous model version of Keller et al. (2012) to identify the changes that result from including a dynamic iron cycle.

### 3.1 The iron cycle

The new model with a dynamic iron cycle allows us to provide an estimate of global marine iron fluxes between major biogeochemical pools (Fig. 3). With the deposition forcing from Luo et al. (2008) the atmospheric iron deposition is a source of 2.1 Gmol Fe yr<sup>-1</sup> to the ocean. Sedimentary iron release is one order of magnitude higher than iron deposition on the global scale, confirming the important role of the sediment in supplying iron to the ocean as already suggested by prior studies (Moore and Braucher, 2008; Tagliabue et al., 2009). The sediment release of 18.8 Gmol yr<sup>-1</sup> in our model is however still smaller than the 32.5 Gmol yr<sup>-1</sup> of Misumi et al. (2014). Sixty three percent of the iron that is taken up by phytoplankton is recycled back to the dissolved iron pool. This compares well with observations of a large proportion of recycled to new iron sources (Boyd and Ellwood, 2010). The largest simulated flux is scavenging, which is even slightly larger than the remineralization of iron. Although some of the parameters are poorly constrained and, hence, there is some uncertainty in the magnitude of the fluxes, these results emphasize the difference between the iron cycle and macronutrient cycles since the residence time of iron in the ocean as computed from global inventory divided by global iron supply, which results to approximately 38 years here, is orders of magnitude shorter than the millennial residence time scales of the macronutrients nitrogen or phosphorus (Wallmann, 2010; Somes et al., 2013). This indicates that iron concentrations must be strongly dependent on local or regional sources. Our estimate of the iron residence time is within the range of other estimates of 12 years (Moore and Braucher, 2008) and 100 to 200 years (Boyd and Ellwood, 2010). The short residence time illustrates the potentially large leverage that changes in the Fe supply could have on marine biogeochemical cycles.

In comparison to the iron concentration mask used in the previous model version, the dynamically simulated surface iron concentrations in the new model are generally

## A dynamic marine iron cycle for the UVic model

L. Nickelsen et al.

Title Page

Abstract

Introduction

Conclusions

References

Tables

Figures



Back

Close

Full Screen / Esc

Printer-friendly Version

Interactive Discussion



## A dynamic marine iron cycle for the UVic model

L. Nickelsen et al.

Title Page

Abstract

Introduction

Conclusions

References

Tables

Figures



Back

Close

Full Screen / Esc

Printer-friendly Version

Interactive Discussion



higher (Fig. 4). This is due to the higher stability constant of iron ligand complexes of  $\log(K_{FeL}) = 11.5$  here compared to the values of 9.8 to 10.8 used in the model of Galbraith et al. (2010), from which the iron mask in Keller et al. (2012) had been taken. Our choice is more in line with recent observational estimates of  $\log(K_{FeL})$  being in the range of 11–12 (Gledhill and Buck, 2012). An additional factor could be the linear dependence of inorganic scavenging on free iron concentrations in the model presented here (cf. Eq. 23) which differs from the scaled (to the power of 1.5) inorganic scavenging of free iron in the model of Galbraith et al. (2010). Since our new formulation results in less scavenging the surface iron concentrations are slightly overestimated in the subtropical North Pacific, the tropical Atlantic and possibly the Indian Ocean as well as the Arctic Ocean. However, the global root mean square error (RMSE), relative to observed surface iron concentrations (Tagliabue et al., 2012), decreases from 0.81 to 0.69 nM when compared to the surface iron concentrations of the iron concentration mask used by Keller et al. (2012), e.g., the regrided results of the BLING model (Galbraith et al., 2010).

The simulated zonal mean iron concentrations reveal that the iron concentrations in the Southern Ocean are probably a little too high, particular in the Pacific (Fig. 5). However, the model does capture the high iron concentrations that have been observed in the northern Indian Ocean, as well as elevated iron concentrations in the North Pacific and North Atlantic. The highest observed dissolved iron concentrations of up to 1.5 nM can not be represented by the model because of the globally constant ligand concentration of 1 nM which is probably too low in the regions of high iron concentrations (Gledhill and Buck, 2012). This indicates that a more detailed understanding of sources and sinks of ligands is necessary to better represent dissolved iron concentrations.

The deviation of the profile of dissolved iron to the observations (Fig. 6) could be due to the constant and maybe too low ligand concentration in the model and supports the notion that there is still no comprehensive understanding of sources and sinks of ligands although some promising approaches are emerging (Misumi et al., 2013). The other model tracers shown in Fig. 6 are discussed in the next section.

## A dynamic marine iron cycle for the UVic model

L. Nickelsen et al.

[Title Page](#)[Abstract](#)[Introduction](#)[Conclusions](#)[References](#)[Tables](#)[Figures](#)[Back](#)[Close](#)[Full Screen / Esc](#)[Printer-friendly Version](#)[Interactive Discussion](#)

5 Simulated surface iron concentration show a seasonal variability that appears somewhat smaller than can be inferred from the available data (Fig. 7). In the Northern Hemisphere simulated iron concentrations between 40 and 60° N start to get depleted in April. This is associated with the spring and summer bloom in the Northern Hemisphere. At the same time iron concentrations in the Southern Ocean start to increase showing that, as also stated by Tagliabue et al. (2014b), supply of iron to the surface from the deeper ocean during austral winter is an important source of iron.

10 In summary, the new dynamic iron cycle model allows identification of the important fluxes between the iron pools, indicates that more research is needed on ligand dynamics and shows a clear improvement over the iron concentration masking approach that was used previously with UVic. In comparison to the model by Misumi et al. (2013), who also compare their simulated iron concentrations to the full dataset by Tagliabue et al. (2012) and calculated a RMSE of 0.78 nM at the surface and 0.86 nM in the deep (200–5000 m) ocean, we get lower RMSEs of 0.68 nM at the surface and 0.60 nM for the full ocean.

15 One difficulty that we faced in evaluation of our results is that the observations of iron concentrations are still sparse and show high variability. The observed concentrations in the Southern Ocean are probably biased towards concentrations in the austral summer due to easier sampling at that time of the year. The available observations are highly valuable but more observations of iron concentrations are needed for better understanding and evaluation of model results.

### 3.2 Biogeochemical validation

25 Having a dynamic iron cycle induces changes in all other simulated biogeochemical properties. Here we compare the biogeochemical results of these new simulations to the observations and previous model and discuss the reasons for them.

In comparison to the previous model version, surface  $\text{PO}_4$  and  $\text{NO}_3$  in the Southern Ocean are slightly lower due to the higher iron concentrations and reduced Fe limitation (Fig. 8). In the equatorial Pacific the  $\text{PO}_4$  concentrations are higher in the

## A dynamic marine iron cycle for the UVic model

L. Nickelsen et al.

Title Page

Abstract

Introduction

Conclusions

References

Tables

Figures



Back

Close

Full Screen / Esc

Printer-friendly Version

Interactive Discussion



subtropical gyres, which are the regions where iron concentrations are smaller than 0.1 nM (Fig. 4). This indicates that iron limitation might be too strong there. A further reason could be the not well resolved equatorial current system (Getzlaff and Dietze, 2013). However, the overestimation of phosphate concentrations in the tropical Pacific seen in the previous version is reduced and  $\text{PO}_4$  and  $\text{NO}_3$  are also more in agreement with observations in the North Pacific. In total, surface  $\text{PO}_4$  and  $\text{NO}_3$  RMSEs reduce by  $0.02 \text{ mmol PO}_4 \text{ m}^{-3}$  and  $0.28 \text{ mmol NO}_3 \text{ m}^{-3}$  with the new version.

Changes in the surface nutrient limitation and hence productivity, influence oxygen concentrations via changes in the export of sinking organic matter to the deeper ocean and the subsequent oxygen consumption during remineralization. A common mismatch between observations and simulation results in models with a coarse resolution is that high nutrient concentrations are simulated in the eastern tropical Pacific and subsequently cause large oxygen minimum zones (OMZs), i.e. volumes of low oxygen waters ( $< 5 \text{ mmol m}^{-3}$ ), to be formed at intermediate depths as a result of processes that have been termed “nutrient trapping” (Najjar et al., 1992; Dietze and Loeptien, 2013; Getzlaff and Dietze, 2013). With the new model the area of the OMZ in the eastern tropical Pacific at 450 m depth is reduced while low oxygen concentrations reach further into the western Pacific (Fig. 9). This is more in agreement with observations of low oxygen concentrations. The relatively low oxygen concentrations of around  $190 \text{ mmol m}^{-3}$  in some places of the Southern Ocean and the OMZ in the Indian Ocean can still not be represented by the model. The OMZ is located in the Bay of Bengal instead of the Arabian Sea in both model versions. This is a common model error (Moore and Doney, 2007) and a possible reason is the coarse resolution of these models which might not be able to realistically simulate Indian ocean currents and the transport of nutrients and oxygen. However, in total, also the global oxygen concentrations have a slightly smaller error than in the previous model (Fig. 6).

The global net primary production (NPP) in the ocean is calculated to be  $55 \text{ Pg Cyr}^{-1}$  in the new model while it was  $52 \text{ Pg Cyr}^{-1}$  in the old model. A recent estimate using both, observations and models, is in the same range, stating that  $56 \text{ Pg Cyr}^{-1}$  is the

most probable value for global NPP (Buitenhuis et al., 2013). Spatially, the net primary production in the new model deviates from the net primary production in the previous model mostly in that the production is more centered on the equator in the Pacific Ocean and less production occurs in the eastern tropical Pacific (Fig. 10). The new model also shows higher production downstream of the southern tips of the continents in the Southern Ocean, such as South America, Africa and Australia. Although generally in comparison to the satellite based observational estimates coastal production seems still to be underestimated and open ocean production overestimated (Keller et al., 2012), the production in the equatorial Pacific and eastern tropical Pacific are now more similar to the observations.

These changes in productivity, relative to the old model, affect the simulated biological pump. Lower net primary production in the equatorial and eastern tropical Pacific is mirrored in the export of organic and inorganic matter (POC and PIC fluxes) at 2 km, in contrast to the higher export with the old model (Fig. 11a). Export in the North Pacific also decreases, although it is slightly higher off the coast of Japan. In contrast, export in the Southern Ocean is higher. The change of the flux of particulate inorganic carbon (PIC flux) from the old to the new model is similar to that of the POC flux with decreases in the equatorial and eastern tropical Pacific, North Pacific and increases in the Southern Ocean (Fig. 11b). Accordingly the rain ratio does not change substantially except for the arctic sea but POC and PIC fluxes are very low there so that the ratio is very sensitive to small changes and thus unimportant in a global context (Fig. 11c).

The higher export in the Southern Ocean with respect to the old version also increases deep phosphate concentrations in the Southern Ocean (Fig. 12). Apart from this Southern Ocean increase, zonally averaged phosphate concentrations are very similar to the old model. The global difference of  $\text{NO}_3$  to the old version is similar to that of  $\text{PO}_4$  because the same mechanisms apply except for N fixation and denitrification which are discussed later.

The increased export production in the Southern Ocean with the new model leads to more remineralization at the subsurface ocean and thus reduces oxygen

## GMDD

7, 8505–8563, 2014

### A dynamic marine iron cycle for the UVic model

L. Nickelsen et al.

Title Page

Abstract

Introduction

Conclusions

References

Tables

Figures



Back

Close

Full Screen / Esc

Printer-friendly Version

Interactive Discussion



concentrations (Fig. 13). This is more in line with observations as also shown by difference plots of both models to observations in the Supplement. However, the observed two oxygen minima in the Atlantic Ocean directly south and north of the equator cannot be represented by the old nor the new model, presumably because of physical limitations of the model. A better representation can be achieved by adjusting the isopycnal diffusivity as in Getzlaff and Dietze (2013) and will be implemented in a future version. Globally, the RMSE of the oxygen concentrations is reduced from  $26.64 \text{ mmol O}_2 \text{ m}^{-3}$  with the old model to  $24.77 \text{ mmol O}_2 \text{ m}^{-3}$  with the new model. The improvement also stems from the oxygen concentrations at depths of 2000 to 3000 m in the subtropical Atlantic that are lower in comparison to the old model and thus, again closer to observed values.

The changes in zonal mean alkalinity are also closely linked to changes in export production, but the improvements in alkalinity, in comparison to the observations, take place in different regions than for oxygen (Fig. 14). The lower export production in the equatorial and North Pacific lowers alkalinity at intermediate depths, which thereby increases the agreement between the simulation results and the observations substantially. The improvements in alkalinity and oxygen are also visible in the globally averaged depth profiles of the model tracers in Fig. 6. Except for alkalinity and oxygen, the old and the new model look very similar. Differences between the simulation results and the observations however tend to be smaller with the new model (Fig. 6b).

The iron limitation of diazotrophs is suggested to be a major control of nitrogen fixation and thus on an important source of new oceanic nitrogen (Mills et al., 2004). With the new dynamic iron cycle simulated nitrogen fixation shifts more to the western tropical Pacific, but does also increase near the coast of the eastern tropical Pacific where deeper in the water column denitrification is taking place (Fig. 15). The vicious cycle hypothesis by Landolfi et al. (2013) states that spatially coupled nitrogen fixation and denitrification can lead to substantial loss of nitrogen when enhanced export production by the fixed nitrogen triggers oxygen consumption in deeper waters and thus increases denitrification which in turn increases nitrogen deficiency in upwelling

## A dynamic marine iron cycle for the UVic model

L. Nickelsen et al.

Title Page

Abstract

Introduction

Conclusions

References

Tables

Figures



Back

Close

Full Screen / Esc

Printer-friendly Version

Interactive Discussion



## A dynamic marine iron cycle for the UVic model

L. Nickelsen et al.

Title Page

Abstract

Introduction

Conclusions

References

Tables

Figures



Back

Close

Full Screen / Esc

Printer-friendly Version

Interactive Discussion



water to the surface creating a niche for diazotrophs. Iron limitation at the surface was discussed as a mechanism that interrupts this feedback by shifting the nitrogen fixation to regions of sufficient iron concentrations away from the region of low oxygen concentrations and denitrification. However, the new model shows that near the coast, the spatial coupling of nitrogen fixation and denitrification can take place when the shallow sediments are a strong source of iron sufficient to sustain nitrogen fixation (cf. Fig. 2b). Elevated coastal iron concentrations may thus allow the feedback between nitrogen fixation and denitrification to exist. Indeed, Fernandez et al. (2011) observe N fixation in the eastern tropical Pacific in the area of the OMZ but more observations are needed to decide whether this feedback occurs as indicated by our model.

### 4 Model experiments

Critical assumptions in modeling the iron cycle are associated with the external sources of iron to the water column, atmospheric iron deposition and sediment release (Tagliabue et al., 2014a). Here we show the results of sensitivity tests that evaluate the importance of assuming the spatially variable solubility of iron in dust and the water column depth of sedimentary iron release. We also test the influence of a temperature dependence of sedimentary iron release and perform a climate warming simulation. All experiments except the climate warming simulation are run for 1000 years and the drift in average surface  $\text{PO}_4$  during the last 100 years is less than  $1.2 \mu\text{mol PO}_4 \text{m}^{-3}$ .

Most previous modeling studies have assumed a constant solubility of iron in dust (Moore and Braucher, 2008; Tagliabue et al., 2014a). However, observations show that the solubility of iron in dust can vary significantly and is generally lower in areas of high dust deposition and higher when dust deposition is low (Baker and Croot, 2010). Luo et al. (2008) tested several assumptions on how iron solubility could change during transport in the atmosphere and compared their simulated atmospheric iron deposition to observations of iron deposition. They found that assuming all iron that comes in contact with clouds is slowly converted to soluble iron and that particularly hematite is

## A dynamic marine iron cycle for the UVic model

L. Nickelsen et al.

Title Page

Abstract

Introduction

Conclusions

References

Tables

Figures



Back

Close

Full Screen / Esc

Printer-friendly Version

Interactive Discussion



a source of soluble iron under acidic conditions results in the best agreement to observations. Their simulated iron deposition also reflects the observed trend of increased solubility at sites of low deposition. To test the importance of having variable solubility we performed a simulation in which iron solubility was set to a constant value of 1 % (this is equal to the global average solubility of the standard model run which has variable solubility) and ran the experiment for 1000 years. These results are compared here to the results of the standard model simulation with variable solubility. Although the integrated total iron deposition increases from 2.1 to 17.8 GmolFem<sup>-2</sup>yr<sup>-1</sup>, the changes in surface iron concentrations are small (Figs. 16 and 4). As expected iron concentrations are higher at sites of high dust deposition (+2 nM Fe in the tropical Atlantic and +1 nM Fe in the Arabian Sea) and lower at low dust deposition (−0.1 nM Fe in the tropical Pacific). However, surface phosphate concentrations are essentially unaffected because the iron limited areas are still iron limited and regions in which iron deposition is high are not iron limited in both cases. The only exceptions are based on a slight increase of iron concentrations at the southern tips of Australia (+0.3 nM) and South America (up to +0.2 nM). These are the areas where surface phosphate concentrations decrease. The strongest effect of the consideration of the variable solubility can be seen in the comparison between simulated iron concentrations and the observations where the RMSE increases from 0.68 nM with variable solubility to 0.91 nM with constant solubility. This result supports the observation of variable solubility of iron in dust and the approach of Luo et al. (2008).

The sediment release of iron is a much larger source of iron to the ocean than dust deposition (Tagliabue et al., 2014a), but it is not clear how much iron released from the sediment reaches the surface ocean. One factor determining whether iron from the sediments reaches the surface ocean in coarse resolution global ocean models is that the simulated bathymetry that can deviate quite strongly from the actual bathymetry. As in other models (Moore and Braucher, 2008; Tagliabue et al., 2014a), we use a subgrid-scale bathymetry to correct the depth of the sedimentary iron release to that of a high resolution dataset of ocean depth. To test the importance of this depth correction, we

turned the correction off in our second experiment and ran the model for 1000 years. This leads to much lower surface iron concentrations, more phytoplankton iron limitation (NPP decreases from 55 to 39 PgCyr<sup>-1</sup>) and an accumulation of macronutrients at the ocean surface (Fig. 17). Although the globally integrated release of iron from the sediment increases from 18.8 GmolFeyr<sup>-1</sup> in the control run to 35.5 GmolFeyr<sup>-1</sup> in the experiment due to local feedbacks in the western Gulf of Mexico and north of Indosia (Fig. 17a), iron in the experiment is released deeper and in regions that are not iron limited. This shows that iron released from the sediment is crucial for sustaining iron concentrations at the surface in iron limited regions and that the depth of iron release is an important factor to consider in coarse resolution models. This is not only true for coastal areas but also for the open ocean, where iron from the sediment is often transported.

We scaled the sedimentary iron release with bottom water temperature to introduce temperature dependent remineralization in sediments as it was already applied to remineralization in the water column in the previous model versions. Although physiological adaptation of the benthic microbial community to low temperatures may compensate for some of the positive effect of temperature on remineralization rates (Arndt et al., 2013), lab experiments show that remineralization rates increase up to sevenfold when sediment is incubated at a temperature gradient (Arnosti et al., 1998; Sanz-Lázaro et al., 2011). The exact influence of temperature on remineralization in sediments is thus still unclear (Arndt et al., 2013). Our choice to include the temperature dependence on the sedimentary iron release is mainly motivated by too high simulated iron concentrations in the Southern Ocean without the temperature dependence. For comparison we optimized the ratio of iron released from the sediment and phosphorus in particulate matter that sinks into the sediment ( $\text{Fe} : \text{P}_{\text{sed}} = 0.015 \text{ mol Fe (mol P)}^{-1}$ ) in a simulation without the temperature dependence of the sedimentary iron release to give the best possible agreement to observations and conducted a 1000 year test simulation. While the average observed iron concentrations south of 40° S are 0.52 nM, simulated concentrations are 0.67 nM without and 0.53 nM with the temperature dependence. Both

## A dynamic marine iron cycle for the UVic model

L. Nickelsen et al.

Title Page

Abstract

Introduction

Conclusions

References

Tables

Figures

◀

▶

◀

▶

Back

Close

Full Screen / Esc

Printer-friendly Version

Interactive Discussion



simulations show a reasonable globally averaged vertical profile of dissolved iron while without the temperature dependence the profile appears to be closer to the observations because of generally higher concentrations (Fig. 18a). However, the difference between simulated and observed iron concentrations is smaller in the simulation with temperature dependence, particular in the deep ocean below 3500 m but also from the surface down to 1500 m (Fig. 18b). Generally, the simulation without temperature dependence leads to lower iron concentrations in the tropical ocean, particular in the Indian Ocean and the western Pacific because of shallow water depths, and higher iron concentrations in the higher latitudes compared to the simulation without the temperature dependence. Thus, more phosphate is taken up in the higher latitudes and phosphate concentrations increase in the tropical regions and east of Australia due to increased iron limitation near Australia and in the tropical Pacific. The model without the temperature dependence and  $\text{Fe} : \text{P}_{\text{sed}} = 0.015 \text{ mol Fe (mol P)}^{-1}$  can be seen as an alternative configuration. Since the agreement to observations is better with temperature dependent sedimentary iron release we made this formulation the standard formulation. However, more observations and experiments of the temperature dependence of benthic remineralization are needed to verify our assumption.

Finally, we performed global warming scenario simulations with the old and the new model and analyzed the response of the ocean. The other components of the Earth system appear to be nearly not influenced by the inclusion of the dynamic iron cycle and the general response of the model to climate warming has already been analyzed in Eby et al. (2013), Zickfeld et al. (2013), and Keller et al. (2014). We ran both models from the 10 000 year long spinups for an additional 200 years during which the atmospheric  $\text{CO}_2$  concentration was allowed to change. Then, we started the emissions driven climate change scenario in the year 1765 and ran the model to year 2100. The  $\text{CO}_2$  emissions follow historical observations to the year 2000 and then a high- $\text{CO}_2$  emissions representative concentration pathway (RCP 8.5) scenario (Meinshausen et al., 2011). Changes in land use, volcanic and solar forcing, aerosols and other greenhouse gases are held constant in our simulations. The global warming

## A dynamic marine iron cycle for the UVic model

L. Nickelsen et al.

[Title Page](#)[Abstract](#)[Introduction](#)[Conclusions](#)[References](#)[Tables](#)[Figures](#)[Back](#)[Close](#)[Full Screen / Esc](#)[Printer-friendly Version](#)[Interactive Discussion](#)

scenario simulations with the old and new models do not differ much in terms of atmospheric CO<sub>2</sub> concentrations (Fig. 19) as it is only 1.2 μatm lower in the year 2100 with the new model than with the old. The inclusion of a dynamic iron cycle does thus not alter the oceanic CO<sub>2</sub> exchange in our model during a climate change simulation on this time scale. However, export production is decreasing faster with the new model during the time from 1765 to 2100. At the same time NPP decreased from 54.82 to 50.98 PgCyr<sup>-1</sup> with the new model and only from 53.70 to 51.90 PgCyr<sup>-1</sup> with the old model. This stronger decrease is due to the increasing iron limitation in the iron limited regions such as the Southern Ocean, equatorial Pacific and North Pacific. The changes in iron limitation are caused by stronger stratification which increases iron concentrations at regions of high dust deposition but decreases iron in regions where supply from the deep ocean is dominant (Fig. 19c).

During the climate warming simulation we keep the atmospheric iron deposition constant but the sediment release of iron decreases from 18.8 to 17.8 GmolFe yr<sup>-1</sup> due to the lower amount of organic matter reaching the sediment. The role of O<sub>2</sub> on the sediment release of iron is restricted to areas of O<sub>2</sub> < 5 mmol m<sup>-3</sup> in our model which, in our model, decrease globally under global warming as in (Duteil and Oschlies, 2011). While scavenging and remineralization increase by 7.4 and 1.0 GmolFe yr<sup>-1</sup>, iron recycling, uptake and grazing/lysis decrease by 1.9 GmolFe yr<sup>-1</sup>, 3.0 and 1.1 GmolFe yr<sup>-1</sup>, respectively, during the simulations from 1765 to 2100. This is caused by the higher stratification, leading to lower iron concentrations in the euphotic zone and higher concentrations below. Together this shows that the response of the dynamic iron cycle to the CO<sub>2</sub> emission scenario has a limited impact on the atmospheric CO<sub>2</sub> concentration, but that the changes of iron concentration can be strong and possibly lead to changes in ocean biogeochemistry on longer time scales.

## GMDD

7, 8505–8563, 2014

### A dynamic marine iron cycle for the UVic model

L. Nickelsen et al.

Title Page

Abstract

Introduction

Conclusions

References

Tables

Figures



Back

Close

Full Screen / Esc

Printer-friendly Version

Interactive Discussion



## 5 Conclusions

Including a dynamic iron cycle leads to a better agreement between observed and simulated iron concentrations than with the iron concentration mask used in the previous model (Keller et al., 2012). The iron cycle now also responds dynamically and interactively with the ocean biogeochemistry to possible perturbations. The improvement of the iron cycling model, when compared to other models such as the one by Misumi et al. (2013), is in part due to better constrained parameters, for example by Gledhill and Buck (2012). Since many fluxes and parameters of the iron cycle are still unconstrained, more observations are necessary, particular ones associated with scavenging since it is the largest flux in the iron cycle.

Many studies have focused on dust deposition as the dominant source of iron to the ocean (Parekh et al., 2008; Tagliabue et al., 2008; Oka et al., 2011), while recently sediment release of iron has been suggested to also be highly important (Moore and Braucher, 2008; Tagliabue et al., 2009, 2014a). We add to these results with our experiments regarding the variable solubility of iron in dust, the temperature dependence of sedimentary iron release and the depth correction of iron release from the sediment. Although variable solubility of iron has a strong impact on the iron concentrations simulated by our model, its effect on macronutrient concentrations is small because it primarily alters iron concentrations in regions that are not iron limited. On the other hand, the subgridscale bathymetry for sedimentary iron release has a very strong impact on both iron concentrations and macronutrients because sediment release is the dominant source of iron in iron limited regions such as the Southern Ocean and eastern tropical Pacific in our model. The temperature dependence of the sedimentary iron release primarily leads to a better agreement between simulated and observed dissolved iron concentrations in the Southern Ocean. Changes in the sediment source can thus potentially drive strong changes in iron limitation at the surface and more observations on what controls sedimentary iron release are crucial.

# GMDD

7, 8505–8563, 2014

## A dynamic marine iron cycle for the UVic model

L. Nickelsen et al.

Title Page

Abstract

Introduction

Conclusions

References

Tables

Figures



Back

Close

Full Screen / Esc

Printer-friendly Version

Interactive Discussion



## A dynamic marine iron cycle for the UVic model

L. Nickelsen et al.

Title Page

Abstract

Introduction

Conclusions

References

Tables

Figures



Back

Close

Full Screen / Esc

Printer-friendly Version

Interactive Discussion



The dynamic response of the iron cycle also allows us to investigate its response to climate change. A previous study found that physical changes in ocean circulation could influence iron supply in iron limited regions (Misumi et al., 2014). However, the largest external source of iron, the release of iron from the sediments, is constant in their model. Due to the strong control of iron released from the sediments on surface iron limitation shown earlier, the response of the sedimentary iron release to climate change could contribute largely to changes of iron concentration and primary production. Sediment release of iron depends on organic matter reaching the sediment, temperature and bottom water oxygen concentrations in our model, all of which change during climate change. Particularly changes in oxygen concentrations could influence iron release from the sediment and could, in turn, also be influenced by iron limitation at the ocean surface. Lower iron limitation could lead to higher export of organic matter and oxygen consumption during respiration. The possible interaction between oxygen and iron concentrations and parameterizations of iron release from the sediment are thus worth to be investigated further.

### Model code availability

The University of Victoria Earth System Climate Model version 2.9 (2009) together with a readme file is available at <http://www.climate.uvic.ca/model/>. The complete files of the model code of the model version used in this paper that are different to files at <http://www.climate.uvic.ca/model/> are available in the Supplement together with additional forcing files. Please see the readme file in the supplement for further instructions on how to use the code. In addition, the model output of the last 1000 years which is used to create the plots and restart files after 9000 and 10 000 years of the 10 000 year spinup are provided at [https://thredds.geomar.de/thredds/fileServer/peerReviewData/nickelsen-et-al\\_gmd\\_2014/Nickelsen-et-al\\_GMD\\_2014\\_submitted.zip](https://thredds.geomar.de/thredds/fileServer/peerReviewData/nickelsen-et-al_gmd_2014/Nickelsen-et-al_GMD_2014_submitted.zip).

The Supplement related to this article is available online at  
doi:10.5194/gmdd-7-8505-2014-supplement.

*Acknowledgements.* We acknowledge financial support from the Deutsche Forschungsgemeinschaft (SFB 754). We thank Michael Eby (University of Victoria, Victoria, Canada) for maintaining the code of the UVic model, Natalie Mahowald (Cornell University, Ithaca, USA) for sharing the dust deposition estimates and Heiner Dietze (GEOMAR, Kiel, Germany) for helpful discussions, advice and technical support.

## References

- Arndt, S., Jørgensen, B., LaRowe, D., Middelburg, J., Pancost, R., and Regnier, P.: Quantifying the degradation of organic matter in marine sediments: a review and synthesis, *Earth-Sci. Rev.*, 123, 53–86, 2013. 8530
- Arnosti, C., Jørgensen, B., Sagemann, J., and Thamdrup, B.: Temperature dependence of microbial degradation of organic matter in marine sediments: polysaccharide hydrolysis, oxygen consumption, and sulfate reduction, *Mar. Ecol.-Prog. Ser.*, 165, 59–70, 1998. 8518, 8519, 8530
- Aumont, O. and Bopp, L.: Globalizing results from ocean in situ iron fertilization studies, *Global Biogeochem. Cy.*, 20, 1–15, doi:10.1029/2005GB002591, 2006. 8513, 8520, 8544
- Baker, A. R. and Croot, P.: Atmospheric and marine controls on aerosol iron solubility in seawater, *Mar. Chem.*, 120, 4–13, doi:10.1016/j.marchem.2008.09.003, 2010. 8528
- Behrenfeld, M. J. and Falkowski, P.: Photosynthetic rates derived from satellite-based chlorophyll concentration, *Limnol. Oceanogr.*, 42, 1–20, 1997. 8554
- Boyd, P. W. and Ellwood, M. J.: The biogeochemical cycle of iron in the ocean, *Nat. Geosci.*, 3, 675–682, doi:10.1038/ngeo964, 2010. 8507, 8522
- Buitenhuis, E. T., Hashioka, T., and Quéré, C. L.: Combined constraints on global ocean primary production using observations and models, *Global Biogeochem. Cy.*, 2012, doi:10.1002/gbc.20074, 2013. 8526
- Cox, P. M.: Description of the TRIFFID dynamic global vegetation model, Technical Report Technical Note, HCTN24, 1–16, available at: [http://www.metoffice.gov.uk/media/pdf/9/h/HCTN\\_24.pdf](http://www.metoffice.gov.uk/media/pdf/9/h/HCTN_24.pdf) (last access: 15 October 2014), 2001. 8509

## A dynamic marine iron cycle for the UVic model

L. Nickelsen et al.

Title Page

Abstract

Introduction

Conclusions

References

Tables

Figures



Back

Close

Full Screen / Esc

Printer-friendly Version

Interactive Discussion



## A dynamic marine iron cycle for the UVic model

L. Nickelsen et al.

Title Page

Abstract

Introduction

Conclusions

References

Tables

Figures



Back

Close

Full Screen / Esc

Printer-friendly Version

Interactive Discussion



Dietze, H. and Loeptien, U.: Revisiting “nutrient trapping” in global coupled biogeochemical ocean circulation models, *Global Biogeochem. Cy.*, 27, 265–284, doi:10.1002/gbc.20029, 2013. 8525

Duteil, O. and Oschlies, A.: Sensitivity of simulated extent and future evolution of marine sub-oxia to mixing intensity, *Geophys. Res. Lett.*, 38, L06607, doi:10.1029/2011GL046877, 2011. 8532

Eby, M., Zickfeld, K., Montenegro, A., Archer, D., Meissner, K. J., and Weaver, A. J.: Lifetime of anthropogenic climate change: millennial time scales of potential CO<sub>2</sub> and surface temperature perturbations, *J. Climate*, 22, 2501–2511, doi:10.1175/2008JCLI2554.1, 2009. 8509

Eby, M., Weaver, A. J., Alexander, K., Zickfeld, K., Abe-Ouchi, A., Cimatoribus, A. A., Crespin, E., Drijfhout, S. S., Edwards, N. R., Eliseev, A. V., Feulner, G., Fichet, T., Forest, C. E., Goosse, H., Holden, P. B., Joos, F., Kawamiya, M., Kicklighter, D., Kienert, H., Matsumoto, K., Mokhov, I. I., Monier, E., Olsen, S. M., Pedersen, J. O. P., Perrette, M., Philippon-Berthier, G., Ridgwell, A., Schlosser, A., Schneider von Deimling, T., Shaffer, G., Smith, R. S., Spahni, R., Sokolov, A. P., Steinacher, M., Tachiiri, K., Tokos, K., Yoshimori, M., Zeng, N., and Zhao, F.: Historical and idealized climate model experiments: an intercomparison of Earth system models of intermediate complexity, *Clim. Past*, 9, 1111–1140, doi:10.5194/cp-9-1111-2013, 2013. 8509, 8531

Elrod, V. A., Berelson, W. M., Coale, K. H., and Johnson, K.: The flux of iron from continental shelf sediments: a missing source for global budgets, *Geophys. Res. Lett.*, 31, 2–5, doi:10.1029/2004GL020216, 2004. 8518, 8519, 8544

Eppley, R.: Temperature and phytoplankton growth in the sea, *Fish. Bull.*, 70, 1063–1085, 1972. 8514

Fernandez, C., Farías, L., and Ulloa, O.: Nitrogen fixation in denitrified marine waters., *PLoS one*, 6, e20539, doi:10.1371/journal.pone.0020539, 2011. 8528

Galbraith, E. D., Gnanadesikan, A., Dunne, J. P., and Hiscock, M. R.: Regional impacts of iron-light colimitation in a global biogeochemical model, *Biogeosciences*, 7, 1043–1064, doi:10.5194/bg-7-1043-2010, 2010. 8508, 8511, 8514, 8515, 8516, 8517, 8518, 8523, 8548

Garcia, H. E., Locarnini, R. A., Boyer, T. P., Antonov, J. I., Baranova, O. K., Zweng, M. M., and Johnson, D. R.: *World Ocean Atlas 2009, Volume 3: Dissolved Oxygen, Apparent Oxygen Utilization, and Oxygen Saturation*, edited by: Levitus, S., NOAA Atlas NESDIS 70, US Government Printing Office, Washington, D.C., p. 344, 2010a. 8521, 8553, 8557

## A dynamic marine iron cycle for the UVic model

L. Nickelsen et al.

Title Page

Abstract

Introduction

Conclusions

References

Tables

Figures



Back

Close

Full Screen / Esc

Printer-friendly Version

Interactive Discussion



Garcia, H. E., Locarnini, R. A., Boyer, T. P., Antonov, J. I., Zweng, M. M., Baranova, O. K., and Johnson, D. R.: World Ocean Atlas 2009, Volume 4: Nutrients (phosphate, nitrate, silicate), edited by: Levitus, S., NOAA Atlas NESDIS 71, US Government Printing Office, Washington, D.C., p. 398, 2010b. 8521, 8552, 8556

5 Geider, R. J., MacIntyre, H. L., and Kana, T. M.: Dynamic model of phytoplankton growth and acclimation: responses of the balanced growth rate and the chlorophyll a:carbon ratio to light, nutrient-limitation and temperature, *Mar. Ecol.-Prog. Ser.*, 148, 187–200, doi:10.3354/meps148187, 1997. 8544

Gent, P. and McWilliams, J.: Isopycnal mixing in ocean circulation models, *J. Phys. Oceanogr.*, 20, 150–155, doi:10.1175/1520-0485(1990)020<0150:IMIOCM>2.0.CO;2, 1990. 8509

10 Getzlaff, J. and Dietze, H.: Effects of increased isopycnal diffusivity mimicking the unresolved equatorial intermediate current system in an earth system climate model, *Geophys. Res. Lett.*, 40, 2166–2170, doi:10.1002/grl.50419, 2013. 8525, 8527

Gledhill, M. and Buck, K.: The organic complexation of iron in the marine environment: a review, *Frontiers in Microbiology*, 3, 1–17, doi:10.3389/fmicb.2012.00069, 2012. 8516, 8517, 8523, 8533, 8544

Honeyman, B. D., Balistrieri, L., and Murray, J.: Oceanic trace metal scavenging: the importance of particle concentration, *Deep-Sea Res.*, 35, 227–246, doi:10.1016/0198-0149(88)90038-6, 1988. 8517

20 Hopkinson, B. and Barbeau, K.: Organic and redox speciation of iron in the eastern tropical North Pacific suboxic zone, *Mar. Chem.*, 106, 2–17, doi:10.1016/j.marchem.2006.02.008, 2007. 8518

Hopkinson, B., Mitchell, B., Reynolds, R., Wang, H., Selph, K., Measures, C. I., Hewes, C., Holm-Hansen, O., and Barbeau, K.: Iron limitation across chlorophyll gradients in the southern Drake Passage: phytoplankton responses to iron addition and photosynthetic indicators of iron stress, *Limnol. Oceanogr.*, 52, 2540–2554, 2007. 8515

Johnson, K., Gordon, R., and Coale, K. H.: What controls dissolved iron concentrations in the world ocean?, *Mar. Chem.*, 57, 181–186, doi:10.1016/S0304-4203(97)00047-9, 1997. 8544

30 Keller, D. P., Oschlies, A., and Eby, M.: A new marine ecosystem model for the University of Victoria Earth System Climate Model, *Geosci. Model Dev.*, 5, 1195–1220, doi:10.5194/gmd-5-1195-2012, 2012. 8508, 8509, 8510, 8512, 8513, 8514, 8515, 8521, 8522, 8523, 8526, 8533, 8544, 8545

## A dynamic marine iron cycle for the UVic model

L. Nickelsen et al.

Title Page

Abstract

Introduction

Conclusions

References

Tables

Figures



Back

Close

Full Screen / Esc

Printer-friendly Version

Interactive Discussion



Keller, D. P., Feng, E. Y., and Oeschles, A.: Potential climate engineering effectiveness and side effects during a high carbon dioxide-emission scenario, *Nature Communications*, 5, 3304, doi:10.1038/ncomms4304, 2014. 8531

Key, R. M., Kozyr, A., Sabine, C. L., Lee, K., Wanninkhof, R., Bullister, J. L., Feely, R. A., Millero, F. J., Mordy, C., and Peng, T.-H.: A global ocean carbon climatology: results from Global Data Analysis Project (GLODAP), *Global Biogeochem. Cy.*, 18, GB4031, doi:10.1029/2004GB002247, 2004. 8521

Landolfi, A., Dietze, H., Koeve, W., and Oeschles, A.: Overlooked runaway feedback in the marine nitrogen cycle: the vicious cycle, *Biogeosciences*, 10, 1351–1363, doi:10.5194/bg-10-1351-2013, 2013. 8527

Large, W. G., Danabasoglu, G., McWilliams, J. C., Gent, P. R., and Bryan, F. O.: Equatorial circulation of a global ocean climate model with anisotropic horizontal viscosity, *J. Phys. Oceanogr.*, 13, 518–536, doi:10.1175/1520-0485(2001)031%3C0518:ECOAGO%3E2.0.CO;2, 2001. 8509

Luo, C., Mahowald, N. M., Bond, T., Chuang, P. Y., Artaxo, P., Siefert, R. L., Chen, Y., and Schauer, J.: Combustion iron distribution and deposition, *Global Biogeochem. Cy.*, 22, 1–17, doi:10.1029/2007GB002964, 2008. 8520, 8521, 8522, 8528, 8529, 8546

Mahowald, N. M., Muhs, D. R., Levis, S., Rasch, P. J., Yoshioka, M., Zender, C. S., and Luo, C.: Change in atmospheric mineral aerosols in response to climate: last glacial period, preindustrial, modern, and doubled carbon dioxide climates, *J. Geophys. Res.*, 111, D10202, doi:10.1029/2005JD006653, 2006. 8520

Mahowald, N. M., Engelstaedter, S., Luo, C., Sealy, A., Artaxo, P., Benitez-Nelson, C., Bonnet, S., Chen, Y., Chuang, P. Y., Cohen, D. D., Dulac, F., Herut, B., Johansen, A. M., Kubilay, N., Losno, R., Maenhaut, W., Paytan, A., Prospero, J. M., Shank, L. M., and Siefert, R. L.: Atmospheric iron deposition: global distribution, variability, and human perturbations, *Annual Review of Marine Science*, 1, 245–278, doi:10.1146/annurev.marine.010908.163727, 2009. 8520

Mahowald, N. M., Kloster, S., Engelstaedter, S., Moore, J. K., Mukhopadhyay, S., McConnell, J. R., Albani, S., Doney, S. C., Bhattacharya, A., Curran, M. A. J., Flanner, M. G., Hoffman, F. M., Lawrence, D. M., Lindsay, K., Mayewski, P. A., Neff, J., Rothenberg, D., Thomas, E., Thornton, P. E., and Zender, C. S.: Observed 20th century desert dust variability: impact on climate and biogeochemistry, *Atmos. Chem. Phys.*, 10, 10875–10893, doi:10.5194/acp-10-10875-2010, 2010. 8520

## A dynamic marine iron cycle for the UVic model

L. Nickelsen et al.

Title Page

Abstract

Introduction

Conclusions

References

Tables

Figures



Back

Close

Full Screen / Esc

Printer-friendly Version

Interactive Discussion



- Martinez-Garcia, A., Sigman, D. M., Ren, H., Anderson, R. F., Straub, M., Hodell, D. A., Jaccard, S. L., Eglinton, T. I., and Haug, G. H.: Iron fertilization of the subantarctic ocean during the last ice age, *Science*, 343, 1347–1350, doi:10.1126/science.1246848, 2014. 8507
- Meinshausen, M., Smith, S. J., Calvin, K., Daniel, J. S., Kainuma, M. L. T., Lamarque, J.-F., Matsumoto, K., Montzka, S. A., Raper, S. C. B., Riahi, K., Thomson, A., Velders, G. J. M., and Vuuren, D. P.: The RCP greenhouse gas concentrations and their extensions from 1765 to 2300, *Climatic Change*, 109, 213–241, doi:10.1007/s10584-011-0156-z, 2011. 8531
- Meissner, K. J., Weaver, A. J., Matthews, H. D., and Cox, P. M.: The role of land surface dynamics in glacial inception: a study with the UVic Earth System Model, *Clim. Dynam.*, 21, 515–537, doi:10.1007/s00382-003-0352-2, 2003. 8509, 8521
- Mills, M., Ridame, C., Davey, M., Roche, J. L., and Geider, R. J.: Iron and phosphorus co-limit nitrogen fixation in the eastern tropical North Atlantic, *Nature*, 429, 292–294, 2004. 8507, 8514, 8527
- Misumi, K., Lindsay, K., Moore, J. K., Doney, S. C., Tsumune, D., and Yoshida, Y.: Humic substances may control dissolved iron distributions in the global ocean: implications from numerical simulations, *Global Biogeochem. Cy.*, 27, 450–462, doi:10.1002/gbc.20039, 2013. 8523, 8524, 8533
- Misumi, K., Lindsay, K., Moore, J. K., Doney, S. C., Bryan, F. O., Tsumune, D., and Yoshida, Y.: The iron budget in ocean surface waters in the 20th and 21st centuries: projections by the Community Earth System Model version 1, *Biogeosciences*, 11, 33–55, doi:10.5194/bg-11-33-2014, 2014. 8522, 8534
- Moffett, J. W., Goepfert, T. J., and Naqvi, S. W. A.: Reduced iron associated with secondary nitrite maxima in the Arabian Sea, *Deep-Sea Res. Pt. I*, 54, 1341–1349, doi:10.1016/j.dsr.2007.04.004, 2007. 8518
- Moore, J. K. and Braucher, O.: Sedimentary and mineral dust sources of dissolved iron to the world ocean, *Biogeosciences*, 5, 631–656, doi:10.5194/bg-5-631-2008, 2008. 8508, 8520, 8522, 8528, 8529, 8533, 8544
- Moore, J. K. and Doney, S. C.: Iron availability limits the ocean nitrogen inventory stabilizing feedbacks between marine denitrification and nitrogen fixation, *Global Biogeochem. Cy.*, 21, 1–12, doi:10.1029/2006GB002762, 2007. 8507, 8514, 8525
- Najjar, R., Sarmiento, J. L., and Toggweiler, J. R.: Downward transport and fate of organic matter in the ocean: simulations with a general circulation model, *Global Biogeochem. Cy.*, 6, 45–76, doi:10.1029/91GB02718, 1992. 8525

**A dynamic marine iron cycle for the UVic model**

L. Nickelsen et al.

Title Page

Abstract

Introduction

Conclusions

References

Tables

Figures



Back

Close

Full Screen / Esc

Printer-friendly Version

Interactive Discussion



Noffke, A., Hensen, C., Sommer, S., Scholz, F., Bohlen, L., Mosch, T., Graco, M., and Wallmann, K.: Benthic iron and phosphorus fluxes across the Peruvian oxygen minimum zone, *Limnol. Oceanogr.*, 57, 851–867, 2012. 8518, 8519, 8520, 8544

Oka, A., Abe-Ouchi, A., Chikamoto, M. O., and Ide, T.: Mechanisms controlling export production at the LGM: effects of changes in oceanic physical fields and atmospheric dust deposition, *Global Biogeochem. Cy.*, 25, 1–12, doi:10.1029/2009GB003628, 2011. 8533

Oschlies, A., and Garçon, V.: An eddy-permitting coupled physical-biological model of the North Atlantic: 1. Sensitivity to advection numerics and mixed layer physics, *Global Biogeochem. Cy.*, 13, 135–160, doi:10.1029/98GB02811, 1999. 8510

Parekh, P., Follows, M. J., and Boyle, E. A.: Modeling the global ocean iron cycle, *Global Biogeochem. Cy.*, 18, GB1002, doi:10.1029/2003GB002061, 2004. 8511, 8516

Parekh, P., Follows, M. J., and Boyle, E. A.: Decoupling of iron and phosphate in the global ocean, *Global Biogeochem. Cy.*, 19, GB2020, doi:10.1029/2004GB002280, 2005. 8511, 8517, 8544

Parekh, P., Joos, F., and Müller, S. A.: A modeling assessment of the interplay between aeolian iron fluxes and iron-binding ligands in controlling carbon dioxide fluctuations during Antarctic warm events, *Paleoceanography*, 23, 1–14, doi:10.1029/2007PA001531, 2008. 8508, 8533

Price, N.: The elemental stoichiometry and composition of an iron-limited diatom, *Limnol. Oceanogr.*, 50, 1159–1171, 2005. 8515

Price, N., Ahner, B., and Morel, F.: The equatorial Pacific Ocean: grazer-controlled phytoplankton populations in an iron-limited ecosystem, *Limnol. Oceanogr.*, 39, 520–534, 1994. 8544

Rijkenberg, M. J. A., Steigenberger, S., Powell, C. F., van Haren, H., Patey, M. D., Baker, A. R., and Achterberg, E. P.: Fluxes and distribution of dissolved iron in the eastern (sub-) tropical North Atlantic Ocean, *Global Biogeochem. Cy.*, 26, GB3004, doi:10.1029/2011GB004264, 2012. 8518

Sabine, C. L., Feely, R., Gruber, N., Key, R. M., Lee, K., Bullister, J. L., Wanninkhof, R., Wong, C. S., Wallace, D. W. R., Tilbrook, B., Millero, F. J., Peng, T.-H., Kozyr, A., Ono, T., and Rios, A. F.: The oceanic sink for anthropogenic CO<sub>2</sub>, *Science*, 305, 367–371, 2004. 8507

Sanz-Lázaro, C., Valdemarsen, T., Marín, A., and Holmer, M.: Effect of temperature on biogeochemistry of marine organic-enriched systems: implications in a global warming scenario., *Ecol. Appl.*, 21, 2664–2677, 2011. 8518, 8519, 8530

**A dynamic marine iron cycle for the UVic model**

L. Nickelsen et al.

[Title Page](#)[Abstract](#)[Introduction](#)[Conclusions](#)[References](#)[Tables](#)[Figures](#)[Back](#)[Close](#)[Full Screen / Esc](#)[Printer-friendly Version](#)[Interactive Discussion](#)

- Schmittner, A., Oschlies, A., Giraud, X., Eby, M., and Simmons, H. L.: A global model of the marine ecosystem for long-term simulations: sensitivity to ocean mixing, buoyancy forcing, particle sinking, and dissolved organic matter cycling, *Global Biogeochem. Cy.*, 19, 1–17, doi:10.1029/2004GB002283, 2005. 8510
- 5 Schmittner, A., Oschlies, A., Matthews, H. D., and Galbraith, E. D.: Future changes in climate, ocean circulation, ecosystems, and biogeochemical cycling simulated for a business-as-usual CO<sub>2</sub> emission scenario until year 4000 AD, *Global Biogeochem. Cy.*, 22, 1–21, doi:10.1029/2007GB002953, 2008. 8508, 8510, 8513, 8514, 8515
- Schmittner, A., Oschlies, A., Matthews, H. D., and Galbraith, E. D.: Correction to “Future changes in climate, ocean circulation, ecosystems, and biogeochemical cycling simulated for a business-as-usual CO<sub>2</sub> emission scenario until year 4000 AD”, *Global Biogeochem. Cy.*, 23, 1–1, doi:10.1029/2009GB003577, 2009. 8515
- 10 Severmann, S., McManus, J., Berelson, W. M., and Hammond, D. E.: The continental shelf benthic iron flux and its isotope composition, *Geochim. Cosmochim. Ac.*, 74, 3984–4004, doi:10.1016/j.gca.2010.04.022, 2010. 8518, 8519
- Simmmons, H. L., Jayne, S. R., Laurent, L. C. S., and Weaver, A. J.: Tidally driven mixing in a numerical model of the ocean general circulation, *Ocean Model.*, 6, 245–263, doi:10.1016/S1463-5003(03)00011-8, 2004. 8509
- Somes, C. J., Schmittner, A., and Altabet, M. A.: Nitrogen isotope simulations show the importance of atmospheric iron deposition for nitrogen fixation across the Pacific Ocean, *Geophys. Res. Lett.*, 37, 1–6, doi:10.1029/2010GL044537, 2010. 8507
- 20 Somes, C. J., Oschlies, A., and Schmittner, A.: Isotopic constraints on the pre-industrial oceanic nitrogen budget, *Biogeosciences Discuss.*, 10, 3121–3175, doi:10.5194/bgd-10-3121-2013, 2013. 8520, 8522
- 25 Tagliabue, A., Bopp, L., and Aumont, O.: Ocean biogeochemistry exhibits contrasting responses to a large scale reduction in dust deposition, *Biogeosciences*, 5, 11–24, doi:10.5194/bg-5-11-2008, 2008. 8508, 8533
- Tagliabue, A., Bopp, L., and Aumont, O.: Evaluating the importance of atmospheric and sedimentary iron sources to Southern Ocean biogeochemistry, *Geophys. Res. Lett.*, 36, 1–5, doi:10.1029/2009GL038914, 2009. 8520, 8522, 8533
- 30 Tagliabue, A., Mtshali, T., Aumont, O., Bowie, A. R., Klunder, M. B., Roychoudhury, A. N., and Swart, S.: A global compilation of dissolved iron measurements: focus on distributions and

## A dynamic marine iron cycle for the UVic model

L. Nickelsen et al.

Title Page

Abstract

Introduction

Conclusions

References

Tables

Figures



Back

Close

Full Screen / Esc

Printer-friendly Version

Interactive Discussion



processes in the Southern Ocean, *Biogeosciences*, 9, 2333–2349, doi:10.5194/bg-9-2333-2012, 2012. 8521, 8523, 8524, 8548, 8549, 8550, 8551, 8560, 8561

Tagliabue, A., Aumont, O., and Bopp, L.: The impact of different external sources of iron on the global carbon cycle, *Geophys. Res. Lett.*, 41, 920–926, doi:10.1002/2013GL059059, 2014a. 8507, 8508, 8528, 8529, 8533

Tagliabue, A., Sallée, J., Bowie, A., Lévy, M., Swart, S., and Boyd, P. W.: Surface-water iron supplies in the Southern Ocean sustained by deep winter mixing, *Nat. Geosci.*, 1–7, doi:10.1038/NGEO2101, 2014b. 8524

Timmermans, K. R., Wagt, B. V. D., and de Baar, H. J. W.: Growth rates, half saturation constants, and silicate, nitrate, and phosphate depletion in relation to iron availability of four large open-ocean diatoms from the Southern Ocean, *Limnol. Oceanogr.*, 49, 2141–2151, doi:10.4319/lo.2004.49.6.2141, 2004. 8513, 8544

US Dept. of Commerce, National Oceanic and Atmospheric Administration, and National Geophysical Data Center: 2-minute Gridded Global Relief Data (ETOPO2v2), available at: <http://www.ngdc.noaa.gov/mgg/global/etopo2.html> (last access: 15 October 2014), 2006. 8520

Wallmann, K.: Phosphorus imbalance in the global ocean?, *Global Biogeochem. Cy.*, 24, 1–12, doi:10.1029/2009GB003643, 2010. 8522

Weaver, A. J., Eby, M., Wiebe, E. C., Bitz, C. M., Duffy, P. B., Ewen, T. L., Fanning, A. F., Holland, M. M., MacFayden, A., Matthews, H. D., Meissner, K. J., Saenko, O., Schmittner, A., Wang, H., and Yoshimori, M.: The UVic Earth System Climate Model: model description, climatology, and applications to past, present and future climates, *Atmos.-Ocean*, 39, 361–428, doi:10.1080/07055900.2001.9649686, 2001. 8509, 8521

Westberry, T., Behrenfeld, M. J., Siegel, D. A., and Boss, E.: Carbon-based primary productivity modeling with vertically resolved photoacclimation, *Global Biogeochem. Cy.*, 22, GB2024, doi:10.1029/2007GB003078, 2008. 8554

Zickfeld, K., Eby, M., Weaver, A. J., Alexander, K., Crespin, E., Edwards, N. R., Eliseev, A. V., Feulner, G., Fichet, T., Forest, C. E., Friedlingstein, P., Goosse, H., Holden, P. B., Joos, F., Kawamiya, M., Kicklighter, D., Kienert, H., Matsumoto, K., Mokhov, I. I., Monier, E., Olsen, S. M., Pedersen, J. O. P., Perrette, M., Philippon-Berthier, G., Ridgwell, A., Schlosser, A., Schneider Von Deimling, T., Shaffer, G., Sokolov, A., Spahni, R., Steinacher, M., Tachiiri, K., Tokos, K. S., Yoshimori, M., Zeng, N., and Zhao, F.: Long-term cli-



## A dynamic marine iron cycle for the UVic model

L. Nickelsen et al.

**Table 1.** Parameters that are new or different from Keller et al. (2012) with parameter name, description, reference, value and unit. If no units are given in the reference column, reference units are equal to model units given in the last column.

Parameter	Description	Reference	Value	Unit
$\alpha_{\min}^{\text{chl}}$	Minimum slope in the photosynthesis–irradiance curve	18.4–73.6 (Geider et al., 1997)	18.4	$\mu\text{g C (g Chl)}^{-1} (\text{W m}^{-2})^{-1} \text{s}^{-1}$
$\alpha_{\max}^{\text{chl}}$	Maximum slope in the photosynthesis–irradiance curve	18.4–73.6 (Geider et al., 1997)	73.6	$\mu\text{g C (g Chl)}^{-1} (\text{W m}^{-2})^{-1} \text{s}^{-1}$
$\theta_{\max}$	Maximum Chl : C ratio, abundant iron	0.007–0.072 (Geider et al., 1997)	0.04	$\text{g Chl (g C)}^{-1}$
$\theta_{\min}$	Minimum Chl : C ratio, extreme iron limitation	0.007–0.072 (Geider et al., 1997)	0.01	$\text{g Chl (g C)}^{-1}$
$k\text{Fe}_{\max}$	Maximum half-saturation constant for iron uptake	0.19–1.14 (Timmermans et al., 2004)	0.4	$\mu\text{mol Fe m}^{-3}$
$k\text{Fe}_{\min}$	Minimum half-saturation constant for iron uptake	0.035 (Price et al., 1994)	0.04	$\mu\text{mol Fe m}^{-3}$
$P_{\max}$	Phytoplankton biomass above which $k\text{Fe}$ increases	0.15 (Aumont and Bopp, 2006)	0.15	$\text{mmol N m}^{-3}$
$k\text{Fe}_D$	Diazotroph half-saturation constant for iron uptake	0.06 (Moore and Braucher, 2008)	0.1	$\mu\text{mol Fe m}^{-3}$
$R_{\text{Fe:N}}$	Fe : N uptake ratio	$5 \mu\text{mol Fe (mol C)}^{-1}$ (Johnson et al., 1997)	66.25	$\mu\text{mol Fe (mol N)}^{-1}$
$L_{\text{T}}$	Total ligand concentration	1 (Parekh et al., 2005)	1	$\mu\text{mol lig m}^{-3}$
$\text{Fe} : P_{\text{sed}}$	Fe : P ratio for sedimentary iron source	$0.072 \text{ mol Fe (mol P)}^{-1}$ (Elrod et al., 2004)	0.004	$\text{mol Fe (mol P)}^{-1}$ at $0^\circ\text{C}$
$K\text{FeL}$	Fe-ligand stability constant	$10^{11}$ – $10^{12}$ (Gledhill and Buck, 2012)	$10^{11.5}$	$(\text{mol lig (l}^{-1}\text{)})^{-1}$
$k\text{Fe}_{\text{org}}$	Organic-matter dependent scavenging rate	0.5 (Parekh et al., 2005)	0.45	$(\text{g C})^{-0.58} (\text{m}^3)^{0.58} \text{d}^{-1}$
$k\text{Fe}_{\text{prp}}$	Inorganic scavenging rate	0.003 (Aumont and Bopp, 2006)	0.005	$\text{d}^{-1}$
$\text{O}_{2\min}$	Minimum $\text{O}_2$ concentration for iron oxidation	5 (Noffke et al., 2012)	5	$\text{mmol O}_2 \text{ m}^{-3}$

Title Page

Abstract

Introduction

Conclusions

References

Tables

Figures



Back

Close

Full Screen / Esc

Printer-friendly Version

Interactive Discussion



## A dynamic marine iron cycle for the UVic model

L. Nickelsen et al.

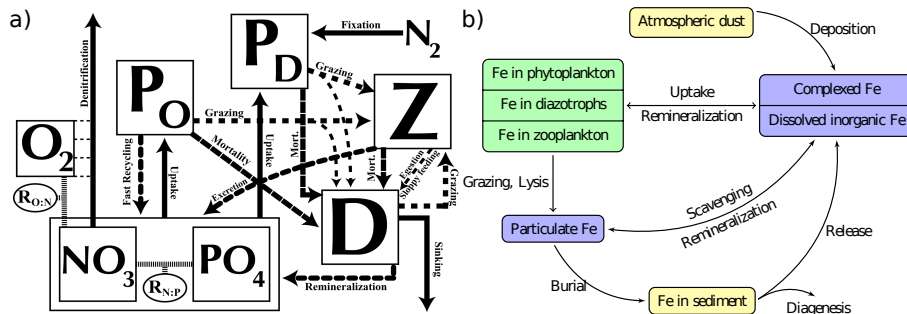


**Figure 1.** (a) Schematic of the previous ecosystem model, which did not include a dynamic iron cycle, illustrating the flux of material between model variables (reprinted from Fig. 1 Keller et al., 2012). (b) Schematic of the new iron cycle that is implemented into the previous model. Assuming that complexation and dissociation are very fast processes, the two new iron tracers are dissolved iron which is assumed to be bioavailable and particulate iron which is assumed to not be bioavailable. Yellow boxes indicate external reservoirs of iron, blue boxes not living iron species in the ocean and green boxes the living iron species in the ocean.

## A dynamic marine iron cycle for the UVic model

L. Nickelsen et al.

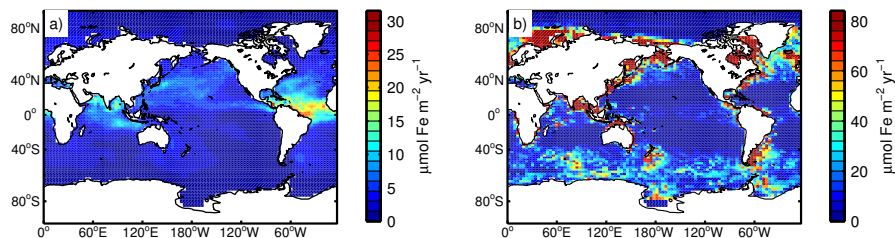


**Figure 2.** Annually averaged atmospheric deposition and sediment release of iron. **(a)** A pre-industrial estimate of climatological annually averaged dust deposition (Luo et al., 2008). **(b)** Sedimentary iron release as simulated with the model according to Eqs. (25) and (26). Note the different color scales.

Title Page

Abstract

Introduction

Conclusions

References

Tables

Figures



Back

Close

Full Screen / Esc

Printer-friendly Version

Interactive Discussion



## A dynamic marine iron cycle for the UVic model

L. Nickelsen et al.

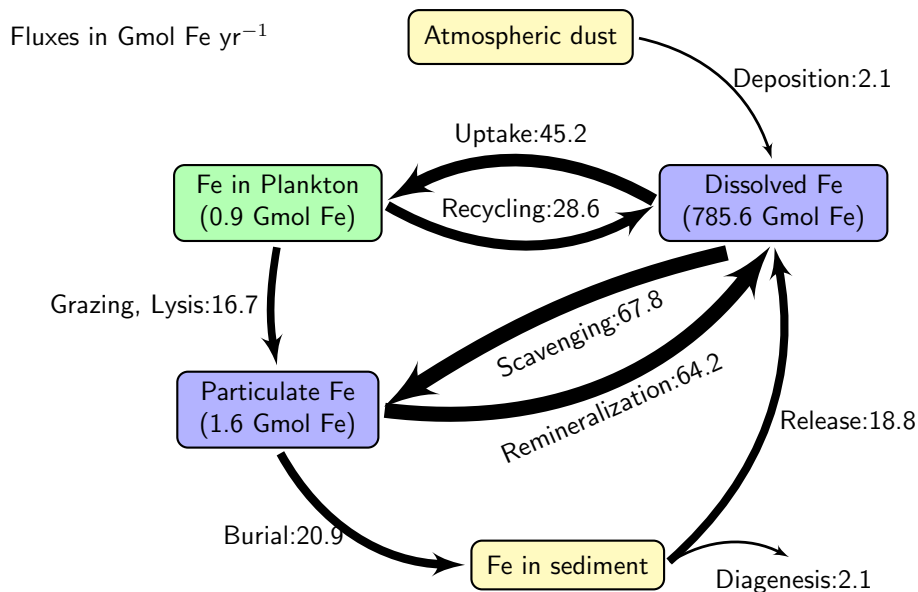


**Figure 3.** Global annually averaged iron fluxes as simulated with the dynamic iron cycle in the UVic model in  $\text{GmolFe yr}^{-1}$ . Arrow thickness is scaled with the size of the fluxes. The numbers inside the boxes denote the globally integrated amounts of iron in the respective pools in  $\text{Gmol Fe}$ .

Title Page

Abstract

Introduction

Conclusions

References

Tables

Figures

◀

▶

◀

▶

Back

Close

Full Screen / Esc

Printer-friendly Version

Interactive Discussion







## A dynamic marine iron cycle for the UVic model

L. Nickelsen et al.

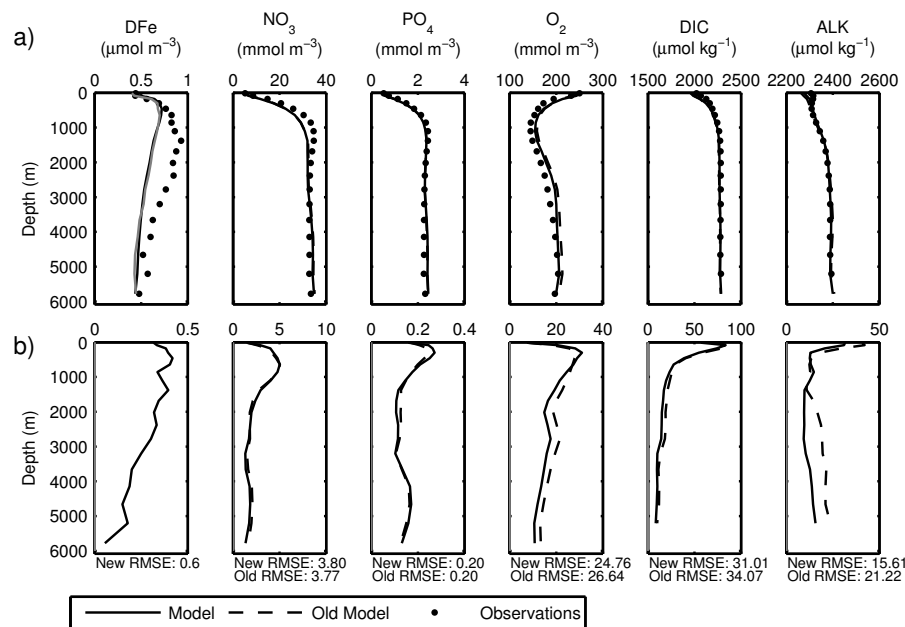


**Figure 6.** Vertical profiles comparing dissolved iron (DFe), nitrate ( $\text{NO}_3$ ), phosphate ( $\text{PO}_4$ ), oxygen ( $\text{O}_2$ ), dissolved inorganic carbon (DIC) and alkalinity (ALK) with observations from Tagliabue et al. (2012), the World Ocean Atlas 2009 and GLODAP (a) and vertical profiles of the horizontally averaged absolute differences between model and the observations (b). The gray line in the profile of dissolved iron is the horizontal average of simulated iron concentrations at the locations of the observations. The global root mean square errors (RMSE) relative to the observations are given below the respective panels in (b).

Title Page

Abstract

Introduction

Conclusions

References

Tables

Figures



Back

Close

Full Screen / Esc

Printer-friendly Version

Interactive Discussion





## A dynamic marine iron cycle for the UVic model

L. Nickelsen et al.

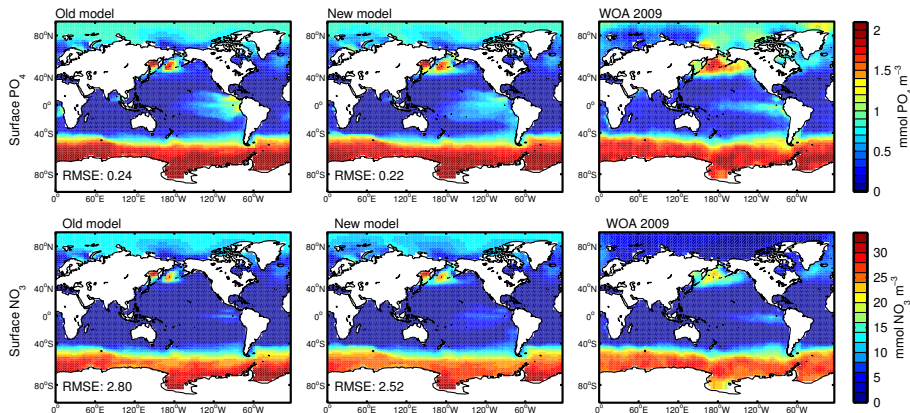


**Figure 8.** Annual mean surface phosphate (first row) and nitrate concentrations (second row) for the old and new model in comparison to observations from the World Ocean Atlas 2009 (WOA, 2009) (Garcia et al., 2010b).

[Title Page](#)[Abstract](#)[Introduction](#)[Conclusions](#)[References](#)[Tables](#)[Figures](#)[⏪](#)[⏩](#)[◀](#)[▶](#)[Back](#)[Close](#)[Full Screen / Esc](#)[Printer-friendly Version](#)[Interactive Discussion](#)

## A dynamic marine iron cycle for the UVic model

L. Nickelsen et al.

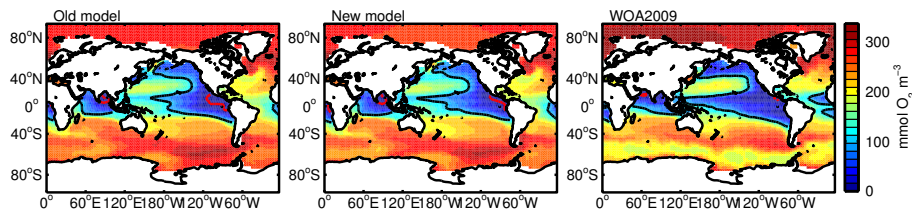


**Figure 9.** Annual mean oxygen concentrations at 450 m depth for the old and new model in comparison to observations from the World Ocean Atlas 2009 (WOA, 2009) (Garcia et al., 2010a). The black contour line is located at concentrations of  $100 \text{ mmol O}_2 \text{ m}^{-3}$ , the red contour line is located at concentrations of  $5 \text{ mmol O}_2 \text{ m}^{-3}$ .

[Title Page](#)[Abstract](#)[Introduction](#)[Conclusions](#)[References](#)[Tables](#)[Figures](#)[◀](#)[▶](#)[◀](#)[▶](#)[Back](#)[Close](#)[Full Screen / Esc](#)[Printer-friendly Version](#)[Interactive Discussion](#)

## A dynamic marine iron cycle for the UVic model

L. Nickelsen et al.

Title Page

Abstract

Introduction

Conclusions

References

Tables

Figures



Back

Close

Full Screen / Esc

Printer-friendly Version

Interactive Discussion

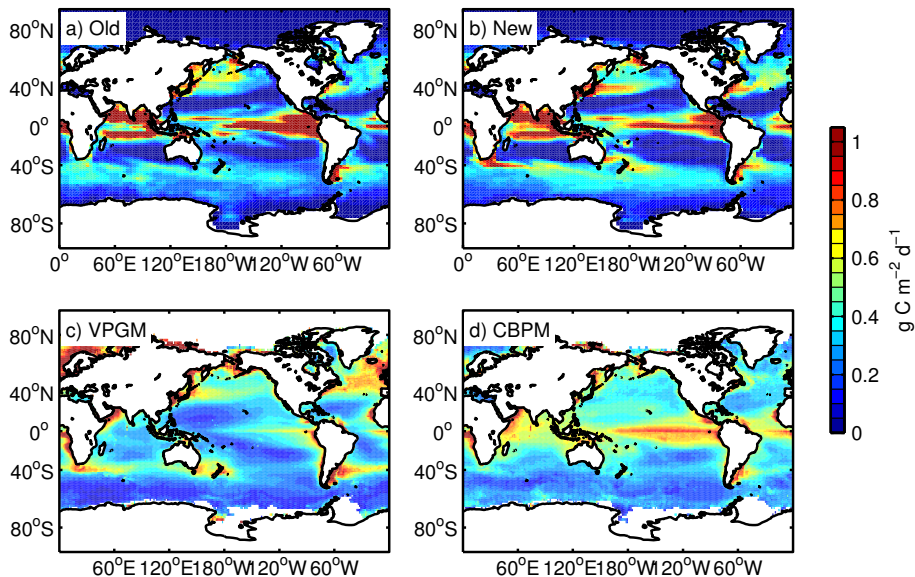


**Figure 10.** Marine vertically integrated annual mean net primary production for **(a)** the old model **(b)** the new model with the dynamic iron cycle, **(c)** the vertically generalized production model (VPGM) by Behrenfeld and Falkowski (1997) and **(d)** the carbon-based productivity model (CBPM) by Westberry et al. (2008).

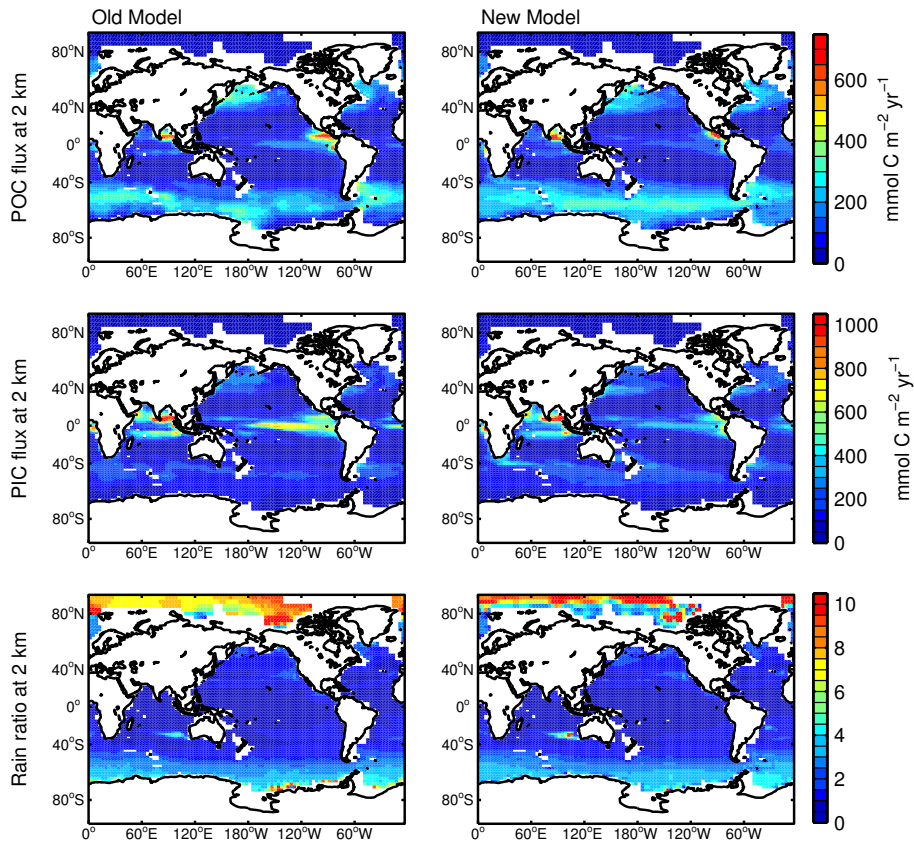


**Figure 11.** Annual fluxes of POC and PIC at 2 km and the rain ratio as simulated with the old model (left column) and with the new model (right column).

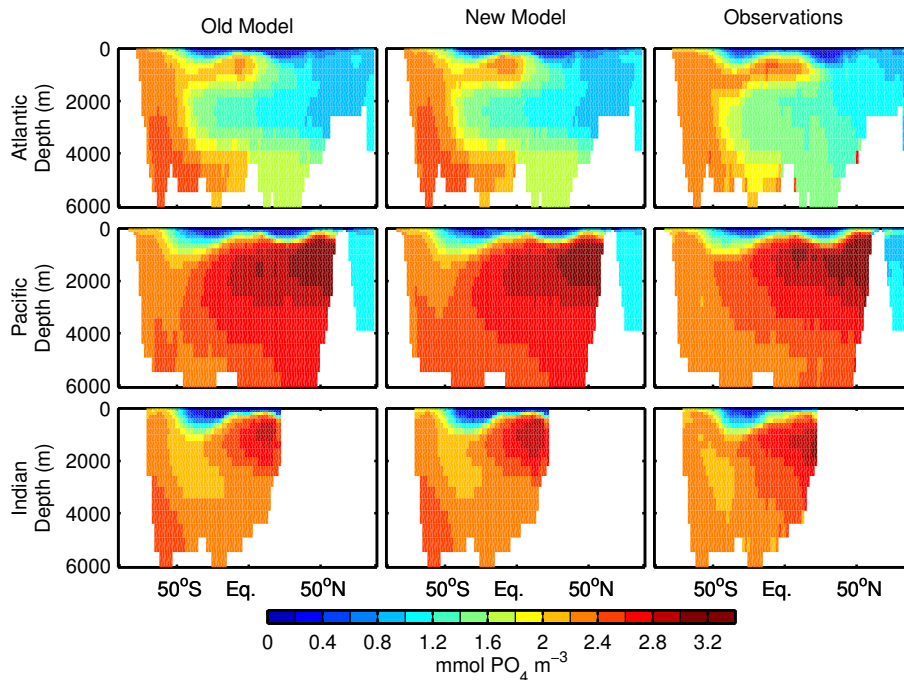


**Figure 12.** Zonal annual mean phosphate concentrations as simulated with the old model (left column) and the new model (middle column) in comparison to observations from the World Ocean Atlas 2009 (WOA, 2009) (Garcia et al., 2010b) (right column) for the different ocean basins.

**A dynamic marine iron cycle for the UVic model**

L. Nickelsen et al.

Title Page

Abstract Introduction

Conclusions References

Tables Figures

◀ ▶

◀ ▶

Back Close

Full Screen / Esc

Printer-friendly Version

Interactive Discussion



## A dynamic marine iron cycle for the UVic model

L. Nickelsen et al.

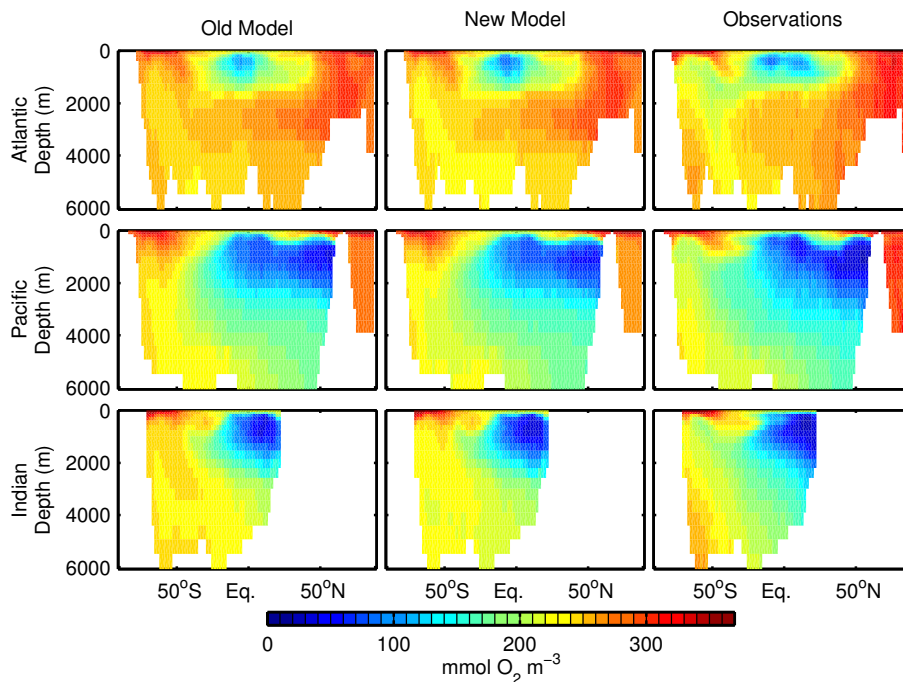


**Figure 13.** Zonal annual mean oxygen concentrations as simulated with the old model (left column) and the new model (middle column) in comparison to observations from the World Ocean Atlas 2009 (WOA, 2009) (Garcia et al., 2010a) (right column) for the different ocean basins.

Title Page

Abstract

Introduction

Conclusions

References

Tables

Figures



Back

Close

Full Screen / Esc

Printer-friendly Version

Interactive Discussion



## A dynamic marine iron cycle for the UVic model

L. Nickelsen et al.

Title Page

Abstract

Introduction

Conclusions

References

Tables

Figures



Back

Close

Full Screen / Esc

Printer-friendly Version

Interactive Discussion

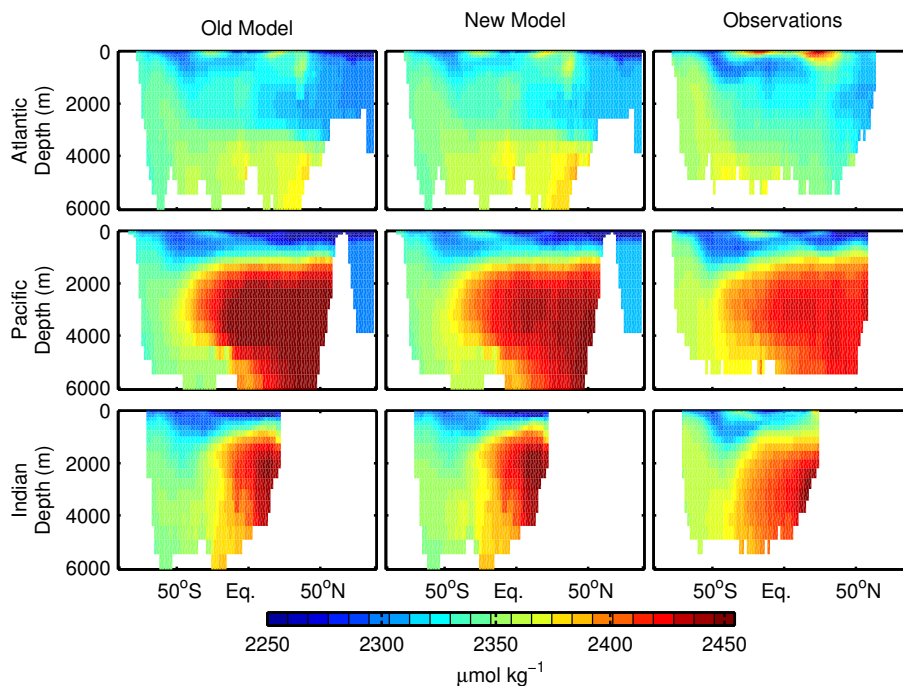


**Figure 14.** Zonal annual mean alkalinity as simulated with the old model (left column) and the new model (middle column) in comparison to observations from GLODAP (right column) for the different ocean basins.

## A dynamic marine iron cycle for the UVic model

L. Nickelsen et al.

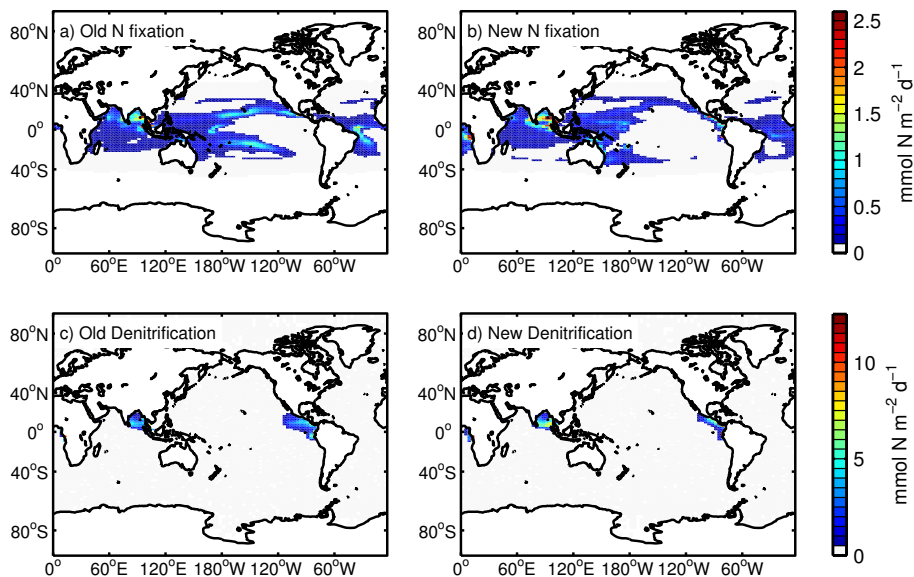


**Figure 15.** Annual mean nitrogen fixation with the old (a) and new model (b) and denitrification with the old (c) and new model (d). Values below  $0.1 \text{ mmol N m}^{-2} \text{ d}^{-1}$  are plotted with white for (a) and (b) while values below  $0.5 \text{ mmol N m}^{-2} \text{ d}^{-1}$  are plotted with white for (c) and (d).

Title Page

Abstract

Introduction

Conclusions

References

Tables

Figures

⏪

⏩

◀

▶

Back

Close

Full Screen / Esc

Printer-friendly Version

Interactive Discussion



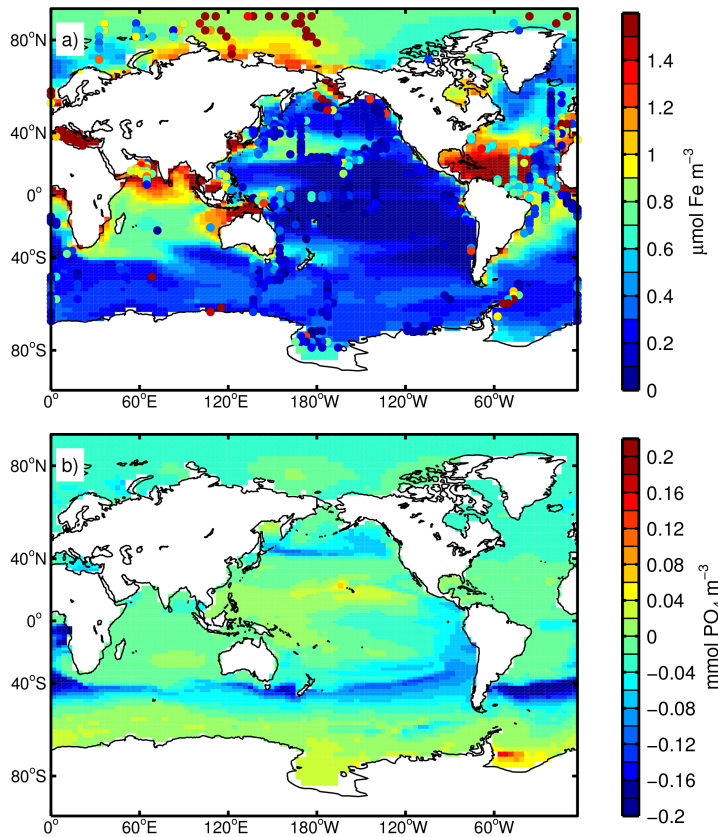


**Figure 16.** Impact of setting the iron solubility in dust to a constant value of 1%. **(a)** Annual mean simulated surface iron concentrations with observations compiled by Tagliabue et al. (2012) plotted as colored circles on top and **(b)** difference of the annual mean surface phosphate concentrations after 1000 years with the iron solubility in dust set to a constant value of 1% to the annual mean surface phosphate concentrations of the standard simulation.

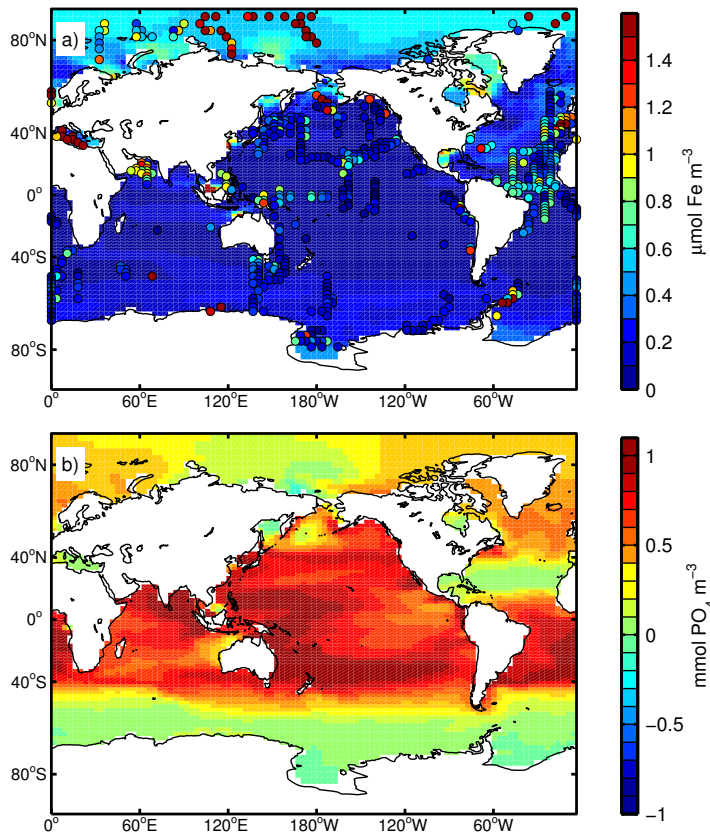


**Figure 17.** Impact of shutting the subgridscale bathymetry after a 1000 year simulation. **(a)** Annual mean simulated surface iron concentrations with the subgridscale bathymetry shut off with observations compiled by Tagliabue et al. (2012) plotted as colored circles on top and **(b)** difference of the annual mean surface phosphate concentrations with the subgridscale bathymetry shut off to the phosphate concentrations of the standard simulation.

## A dynamic marine iron cycle for the UVic model

L. Nickelsen et al.

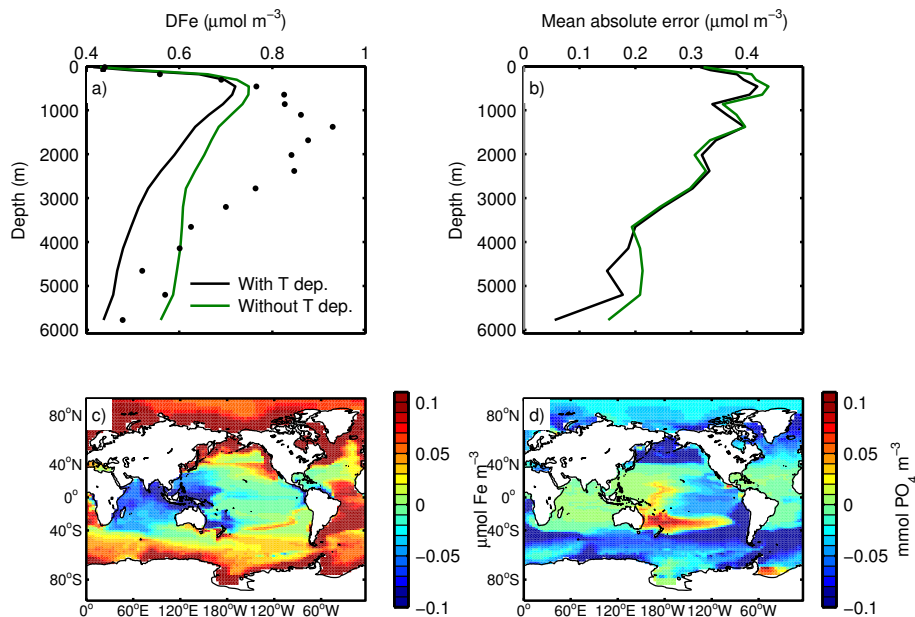


**Figure 18.** iron release. **(a)** Vertical profiles of globally averaged dissolved iron concentrations (dFe) with (black) and without (green) the temperature dependence. **(b)** Vertical profile of the averaged absolute deviation between simulated and observed dFe with (black) and without (green) the temperature dependence. **(c)** Difference in surface dissolved iron concentrations and **(d)** difference in surface phosphate concentrations between the simulations without and with the temperature dependence.

Title Page

Abstract

Introduction

Conclusions

References

Tables

Figures



Back

Close

Full Screen / Esc

Printer-friendly Version

Interactive Discussion



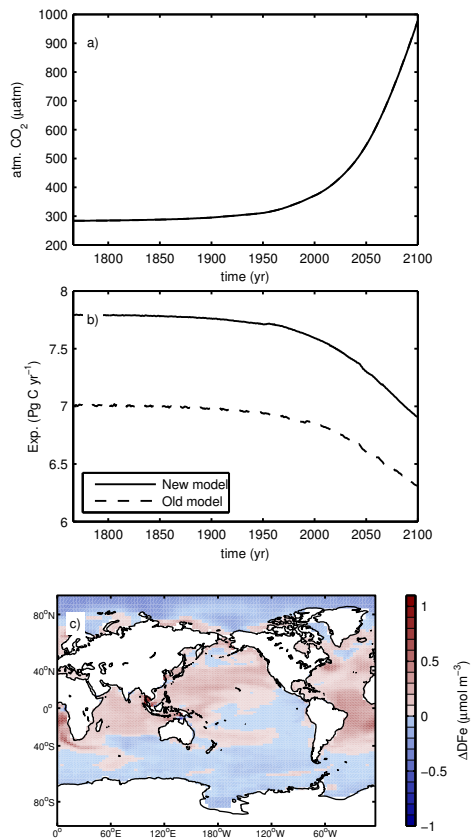


**Figure 19.** Results of the global warming scenario run following the high CO<sub>2</sub> emissions representative concentration pathway (RCP 8.5) scenario: **(a)** Annual average CO<sub>2</sub> concentrations with the new and old model (not distinguishable), **(b)** globally integrated export production at 80m with the new and old model, **(c)** the difference in surface dissolved iron concentrations between the year 2100 and year 1765.